Lithos 320–321 (2018) 75–92

Contents lists available at ScienceDirect

Lithos

journal homepage: www.elsevier.com/locate/lithos

Petrogenesis of gabbroic intrusions in the Valerianov-Beltau-Kurama magmatic arc, Uzbekistan: The role of arc maturity controlling the generation of giant porphyry Cu—Au deposits

Zhiguo Cheng [a], Zhaochong Zhang [a,*], A. Turesebekov [b], B.S. Nurtaev [b], Lijuan Xu [a], M. Santosh [a,c]

[a] State Key Laboratory of Geological Processes and Mineral Resources, China University of Geosciences, Beijing 100083, China
[b] Academy of Sciences of Uzbekistan, Institute of Geology and Geophysics, Tashkent 100041, Uzbekistan
[c] Department of Earth Sciences, University of Adelaide, Adelaide, SA 5005, Australia

ARTICLE INFO

Article history:
Received 29 April 2018
Accepted 31 August 2018
Available online 05 September 2018

Keywords:
Gabbro
Almalyk orefield
Porphyries Cu—Au deposits
Central Asian Orogenic Belt
Arc maturity

ABSTRACT

Arc maturity is considered to play an important role in the mineralization of porphyry Cu—Au deposits. However, the early stage of arc is rarely preserved leading to controversies over arc evolution. Here we investigate gabbroic intrusions from the Akcha, Beleuti and Kalmakyr arc in relation to the Almalyk porphyry Cu—Au orefield in Uzbekistan. The Akcha biotite gabbro shows medium to fine grained texture, and is composed of plagioclase and biotite with minor clinopyroxene, orthopyroxene, quartz and magnetite. The Beleuti and Kalmakyr gabbros display coarse-grained texture, and are dominated by plagioclase, amphibole and clinopyroxene. Zircon LA-ICP-MS U—Pb dating yields ages of 339.9 ± 2.0 Ma for Akcha biotite gabbro, 339.0 ± 3.3 Ma for Beleuti gabbro and 335.0 ± 2.4 Ma for Kalmakyr gabbro. The emplacement ages of these intrusions are older than those of ore-bearing porphyries in the Almalyk orefield, indicating that the gabbros were emplaced during early stage of the arc evolution. The gabbroic rocks are characterized by high Mg# [100 × molar $Mg^{2+}/(Mg^{2+}+Fe^{2+})$, 41–61], low SiO_2 contents (41.6–50.9 wt%), enrichment in large-ion lithophile elements and negative anomalies for high field strength elements, together with relatively depleted Sr-Nd-Hf isotopic compositions (0.7044–0.7057, −1.59-1.96, 3.38–9.96, respectively). The geochemical features suggest that these rocks were mostly derived from the partial melting of mantle wedge modified by subduction-related fluids. Estimates on water contents based on the composition of amphibole show 4.9–5.3 wt% for the Akcha biotite gabbro, and 5.6–6.8 wt% for the Beleuti gabbro. The oxygen fugacity estimated by zircon Ce/Nd, Ce^{4+}/Ce^{3+} ratios are lower than those of porphyries from the giant porphyry deposits in the Central Asian Orogenic Belt. Our results, together with previously reported data on porphyries in the Almalyk orefield suggest that the gabbro was formed in an immature arc setting associated with the northward subduction of the Paleo-Turkestan oceanic plate, whereas the ore-bearing porphyries were formed in a mature arc.

1. Introduction

Porphyry type deposits are important reserves of metals, including approximately 75% copper, 90% molybdenum and almost all rhenium in the world (Sillitoe, 2010). However, their mechanism of formation and tectonic setting are disputed with diverse models proposed including normal oceanic island arc and active continental margin settings, or melts derived from partial melting of subducted plates. Several porphyry deposits are associated with slab-derived melts bearing high initial Cu contents (Sun et al., 2011). In contrast, some studies propose that the generation of porphyry deposits is controlled by a series of processes, such as magma mixing, assimilation, storage and homogenization (MASH; Richards, 2011a). Because of the scarcity of mafic-ultramafic cumulate rocks in most giant porphyry orefields, and the dominance of intermediate-felsic lithologies as the ore-bearing rocks, there is no robust evidence confirming the mantle origin for the ore-bearing magma, which challenges some of the prevailing porphyry Cu—Au or Cu-Mo-Au metallogenic models (Ducea et al., 2015; Kelemen et al., 2014; Rudnick, 1995).

Richards (2003) proposed that arc maturity plays a key role in the formation of porphyry copper deposits. Porphyry systems are mostly generated in a highly mature arc with thickened crust, and are preferentially related to calc-alkalic, rather than tholeiitic magmas (Cooke et al., 2005; Sillitoe, 2010). Chiaradia (2013) presented a compilation of >40,000 published data from 23 Quaternary magmatic arcs worldwide which shows that arc magmas in a thick crust show less clear calc-alkalic evolutionary trend and have lower copper content than those

* Corresponding author.
E-mail address: zczhang@cugb.edu.cn (Z. Zhang).

https://doi.org/10.1016/j.lithos.2018.08.039
0024-4937/

in a thin crust. The missing copper was believed to be retained as sulfides within or under the base of thick arcs, and the initial accumulation of copper favors the formation of porphyry deposits. These studies show that porphyry copper mineralization and island arc maturity are closely linked. However, the early stage of island arc building is often difficult to characterize, and there are no typical examples to understand how the porphyry system evolves with respect to the evolution of the sources and magmas with increasing arc maturity.

Located in the western part of the Central Asian Orogenic Belt (CAOB), the Almalyk porphyry Cu—Au orefield in Uzbekistan represents the second largest porphyry Cu—Au deposit in Asia (Seltmann et al., 2014). Detailed field studies in this region revealed the occurrence of gabbroic intrusions at depth and along the periphery of the orefield, although the nature and tectonic evolution of these rocks remain poorly understood. Previous studies on the Almalyk orefield have focused dominantly on the ore-bearing porphyries, the origin of which has been correlated to the Late Carboniferous subduction of Paleo-Turkestan oceanic plate (e.g. Cheng et al., 2018; Golovanov et al., 2005; Seltmann et al., 2011; Zhao et al., 2017).

In this paper, we report zircon U—Pb ages, mineralogy, major and trace element and Sr-Nd-Hf isotopic compositions for the gabbroic rocks, and propose that these rocks represent the early stage of the magmatic arc. Our study establishes the spatio-temporal patterns of the gabbroic rocks and ore-bearing porphyries, and evaluates the processes of metallogeny associated with the evolution of magmatic arc.

2. Geological setting

The CAOB is one of the largest accretionary orogens in the world, formed by the closure of the Paleo-Asian Ocean. The orogen is composed of a suite of micro-continental blocks, island arcs, and several intervening ocean basins. Its evolution spanned a long period from late Neoproterozoic to middle Mesozoic, separating Siberian Craton from East Europe Craton, Karakum-Tarim Craton and North China Craton (e.g. Allen et al., 1992; Ouyang et al., 2015; Seltmann et al., 2014; Windley et al., 2007; Xiao and Santosh, 2014). The territory of Uzbekistan is predominantly occupied by the Tianshan Mountain system, which is generally divided into three parts, namely Middle Tianshan, South Tianshan and Southwestern Tianshan (Fig. 1; Gao et al., 2009; Biske and Seltmann, 2010; Xiao et al., 2013). Previous studies have reported detailed descriptions of the geological and tectonic history of the CAOB including the Tianshan Mountain system (e.g. Cheng et al., 2018; Long et al., 2011; Mao et al., 2014; Seltmann et al., 2011, 2014; Xiao et al., 2010, 2013; Yang et al., 2012, 2014). The Almalyk orefield is located in the late Paleozoic Valerianov-Beltau-Kurama arc belt along the southern margin of the Middle Tianshan. A brief description of the geology of this region is given below.

The Middle Tianshan region is bound by the Talas-Fergana Fault to the northeast and Turkestan-Atbashi-Inylchek-South Nalati Fault to the south (Biske and Seltmann, 2010; Xue et al., 2014a, 2014b). The northern and southern margins of Middle Tianshan are represented by the late Paleozoic volcano-plutonic belt, superimposed on the Precambrian basement. The Precambrian basement is mainly composed of accretionary material complex comprising dominantly of amphibole-mica schist and marble exposed in the Chatkal area (Biske and Seltmann, 2010; Xue et al., 2014a, 2014b). The sedimentary cover includes metamorphosed marine clastic rocks, carbonate rocks, mafic-felsic volcanic rocks and related pyroclastic rocks ranging in age from Cambrian to Early Permian (Konopelko et al., 2017 and the reference therein).

The Valerianov-Beltau-Kurama arc belt along the southern margin of the Middle Tianshan is an Andean type arc generated by the northern subduction system associated with the closure of Paleo-Turkestan Ocean. It stretches from the Beltau to Kurama ridge and south-western Chatkal and Pskem ridges in Uzbekistan. The arc belt is composed of Precambrian basement, Silurian-Early Devonian granitoids and terrigenous-volcanogenic formation including andesite, dacite, rhyolite, alkali basalt, Carboniferous granitoids (monzonite-diorite-granodiorite, monzonite-granite, diorite, gabbro-syenite) and volcanic rocks (rhyolite, dacite, trachybasalt and trachyandesite), and Permian granitoids and felsic volcanic rocks (Dolgopolova et al., 2016;Konopelko et al., 2017; Seltmann et al., 2011). Recently, Dolgopolova et al. (2016) and Konopelko et al. (2017) conducted detailed studies on these rocks along the Valerianov-Beltau-Kurama arc belt, and identified two paleo-subduction zones. During Silurian-Early Devonian, the Turkestan Ocean subducted northward beneath the Precambrian basement generating the Late Silurian-Early Devonian arc granitoid-volcanic suites. Thereafter, the subduction ceased from Middle Devonian-Early Carboniferous, and the northern side of the Turkestan Ocean was converted to a passive margin with the deposition of thick carbonate and clastic sediments. In the Early Carboniferous, the northward subduction resumed, and voluminous intrusions and volcanic piles were generated. After the Late Carboniferous collision, post-collisional magmatism occurred in Early Permian (Konopelko et al., 2017; Seltmann et al., 2011). Most part of the belt is overlain by thick Mesozoic and Cenozoic sediments. Several important ore deposits of Au, Ag, Cu, Mo, Pb and Zn were generated in the Valerianov-Beltau-Kurama arc belt through hydrothermal processes related to the volcanic and intrusive activities. The deep fault system played an important role in the ore-generation and localization. Most of these faults are south-east and north-west trending with a general width of 25 km or more, and belong to the Middle Tianshan fault systems. The most important Almalyk Cu-Au-Mo orefield includes the Kalmakyr, Sarycheku, Dalnee and other large porphyry copper deposits, Kurgashinkan skarn lead zinc deposit and 21 epithermal gold deposits, constituting the second largest porphyry copper deposit in Asia.

The Akcha biotite gabbro is exposed in the southern part of the Valerianov-Beltau-Kurama arc belt, 70 km west of Tashkent in Uzbekistan (Coordinates: N40°57′23.16″, E 69°49′2.00″) (Fig. 1). The elliptical intrusion extends *E*-W along a strike length of ca. 10 km and is emplaced within Devonian granite (410.6 ± 2.3 Ma, unpublished data), covering an area of ca.15 km^2. The gabbroic intrusion shows chilled margin adjacent to the granitic wall rock. The Beleuti gabbro is exposed in the northeastern Valerianov-Beltau-Kurama arc belt (Coordinates: N41°02′54.48″, E69°41′43.44″), and is exposed around an area of ca.10 km^2. The wall rocks include Silurian and Devonian volcanic rocks, which are in fault contact with the intrusion. Prospecting activities revealed that some mafic intrusions are also present at depth in the Almalyk orefield.

3. Petrography

The Akcha biotite gabbro is medium to fine grained and dominantly composed of ~60–70 vol% plagioclase, ~10–20 vol% biotite, ~5–7 vol% clinopyroxene and ~2–3 vol% orthopyroxene with minor quartz and magnetite (Fig. 2a-c). Plagioclase occurs as euhedral to subhedral tabular grains, ranging in size from 0.2 × 0.5 to 2.5 × 4 mm. Biotite lamellae and range in diameter from 0.2 × 0.5 to 1 × 2 mm. The clinopyroxene occurs as prismatic grains with a size range of 0.2 × 0.4 to 0.5 × 1.2 mm. Orthopyroxene occurs as prismatic grains and shows a size range of 0.4 × 0.7 to 0.6 × 1.0 mm. Quartz is present as subhedral grains, ~0.2 mm in size. Minor magnetite occurs as inclusions in the biotite, whereas most grains are present as anhedral interstitial mineral between plagioclase and biotite. Sulfide minerals such as pyrite and chalcopyrite also occur sporadically.

The Beleuti gabbro is medium to coarse-grained and dark colored, with approximately 50–60 vol% plagioclase, 20–30 vol% amphibole, 5 vol% clinopyroxene, and minor magnetite (Fig. 2d-f). The rocks show typical poikilitic texture with euhedral plagioclase enclosed by anhedral amphibole. Plagioclase occurs as subhedral to euhedral grains with grain size up to 6 mm. Amphibole shows a size range of 0.2 × 0.4 to 4 × 6 mm and occur as acicular to prismatic subhedral grains.

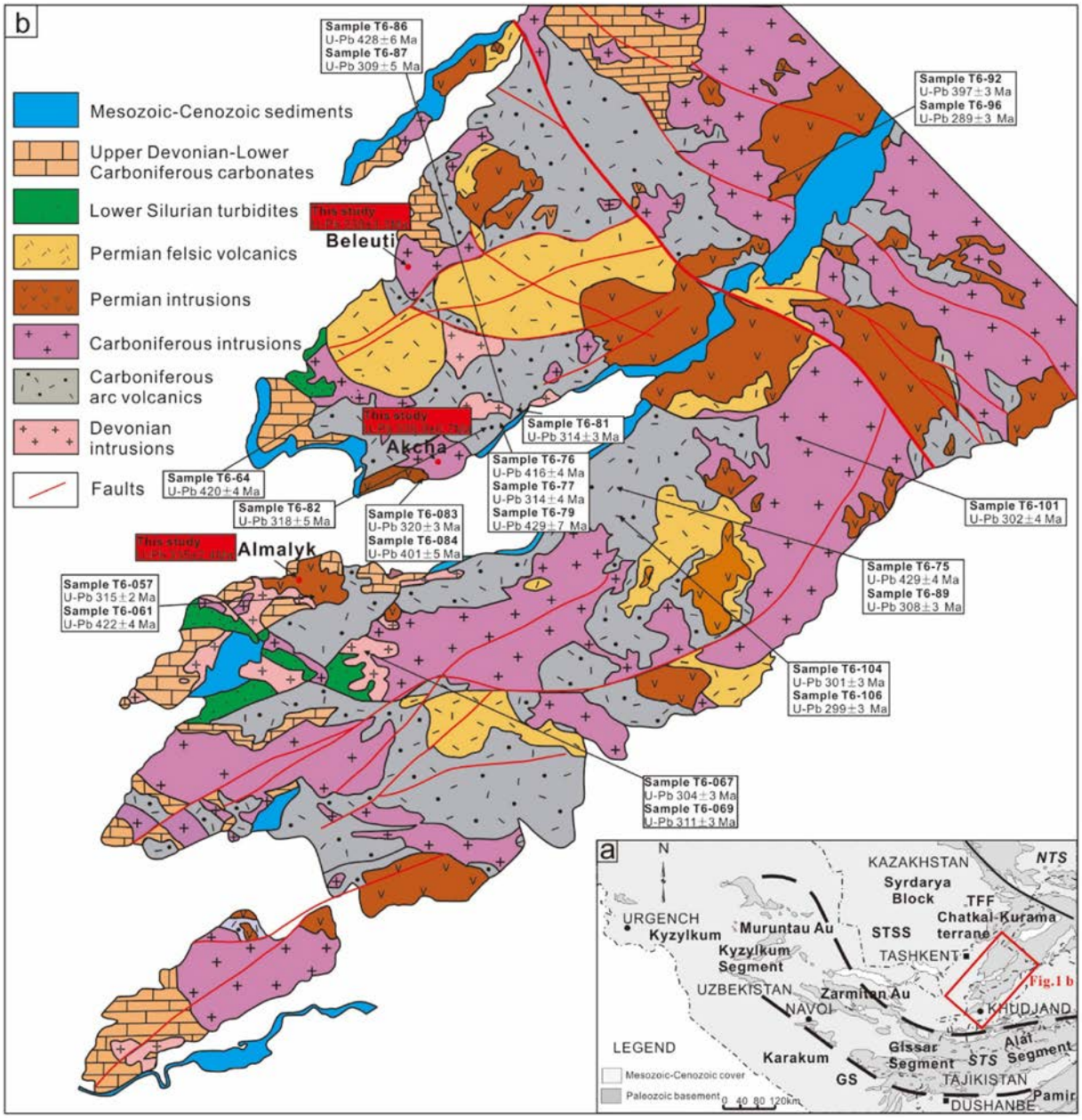

Fig. 1. (a) Simplified geological map of the western TianShan (after Dolgopolova et al., 2016). TFF-Talas-Fergana Fault; STSS-South TianShan suture; GS-Gissar suture; NTS-North TianShan; MTS-Middle TianShan; STS-South TianShan. (b) Schematic geological map of the Chatkal-Kurama terrane showing the Akcha, Beleuti and Almalyk locations. The data shown in open rectangles are from Dolgopolova et al. (2016).

Clinopyroxene is fine grained and enclosed by plagioclase. Magnetite displays a wide range in diameter from ~0.05 to ~0.5 mm, and occurs either as euhedral inclusion in amphibole and plagioclase, or as an anhedral interstitial mineral.

The Kalmakyr gabbro is coarse-grained and shows 50 vol% plagioclase, with size ranging between 1.5 and 6 mm, 40 vol% clinopyroxene (2–4 mm), 7 vol% biotite (0.5–2 mm) and minor magnetite (0.1–0.5 mm) and sulfide (~ 0.2 mm; Fig. 2g-i). Petrographic observation shows that the rocks have been subjected to limited hydrothermal alteration.

4. Sampling and analytical methods

The samples of the Akcha biotite gabbro and Beleuti gabbro were collected from outcrops, whereas those of the Kalmakyr gabbro were obtained from the Institute of Geology and Geophysics, Academy of Sciences of Uzbekistan. Samples were prepared as thin sections for in situ analysis of the major elements. After careful petrographic examination, the rocks were crushed and powdered in an agate mill to a size lower than ~200 mesh for bulk-rock major and trace element, and Sr—Nd isotopic analyses. Zircon grains were separated through conventional heavy liquid and magnetic separation, and handpicking under a binocular microscope. The grains were mounted in 25 mm epoxy resin discs and polished for U—Pb dating and Hf isotopes.

4.1. Mineral chemical analyses

Feldspar, pyroxene, amphibole and biotite were selected for electron microprobe analysis (EMPA). The analysis was performed on polished thin sections at the institute of Mineral Resources, Chinese Academy of Geological Sciences, Beijing using a JXA-8230 electron microprobe with the wavelength dispersive spectrometry. Operating conditions

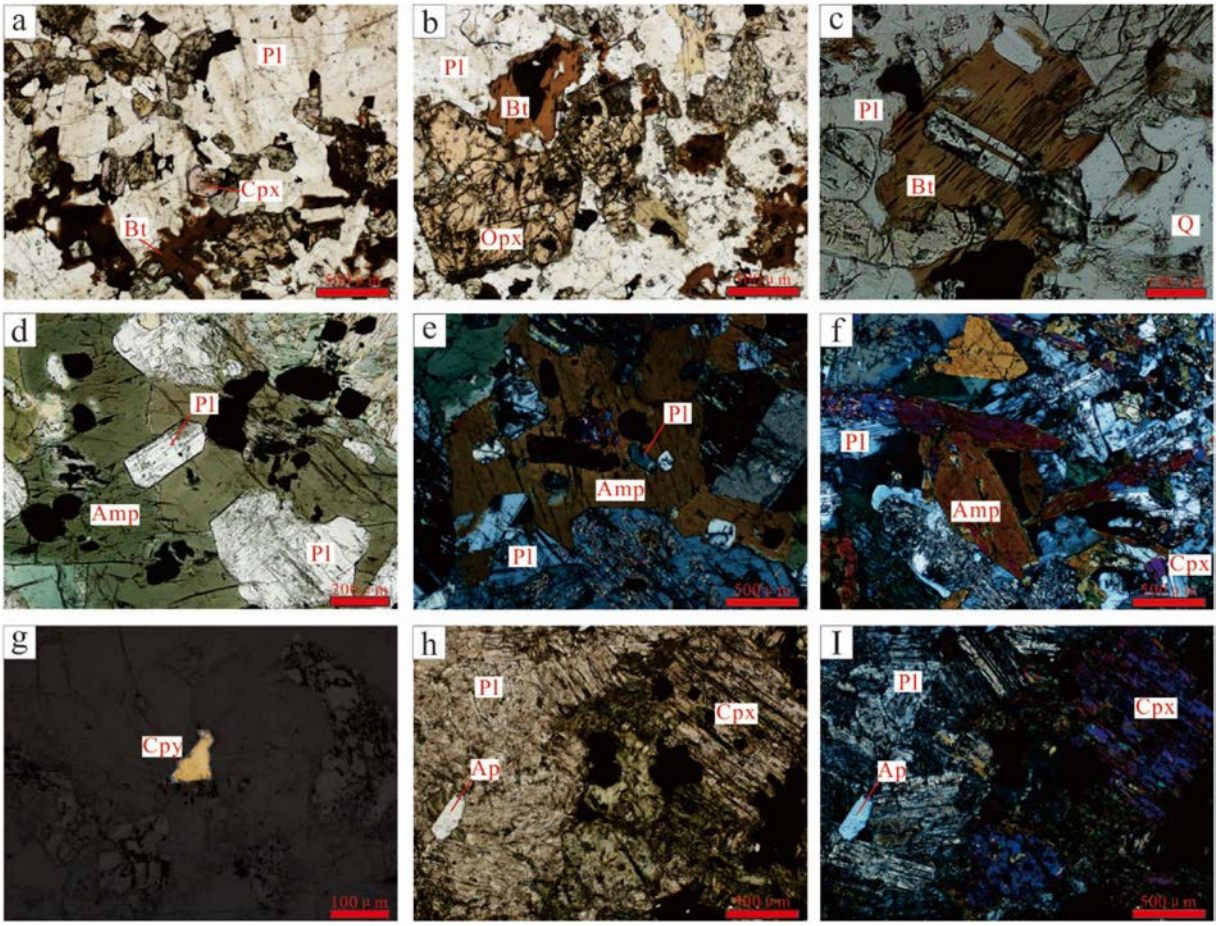

Fig. 2. Photomicrographs of the gabbroic intrusions. (a-c) Akcha biotite gabbro showing medium to fine grained texture, and composed of plagioclase, biotite, clinopyroxene and orthopyroxene, plane-polarized light; (d) Beleuti gabbro displaying medium- to coarse-grained texture, consisting of amphibole and plagioclase, plane-polarized light; (e-f) Beleuti gabbro with medium- to coarse-grained texture, composed of amphibole and plagioclase, crossed-polarized light; (g) Chalcopyrite in the Kalmakyr gabbro, reflected light; (h) Kalmakyr gabbro showing coarse-grained texture, and composed of plagioclase, clinopyroxene, biotite, apatite and minor magnetite, plane-polarized light; (i) Kalmakyr gabbro, crossed-polarized light. Abbreviation: Pl = plagioclase, Bt = biotite, Q = quartz, Amp = amphibole, Cpx = clinopyroxene, Opx = orthopyroxene, Cpy = chalcopyrite, Ap = apatite.

were set at 15kv, 20 nA with a beam of 5 μm, and Na, K, Si, Ca and Fe were analyzed firstly. The standards employed to monitor the analysis process included natural minerals and synthetic oxides. Raw data were corrected by the ZAF method, and the precision for oxide concentrations is better than 1%.

4.2. Zircon U—Pb dating

Zircon grains were separated from the Akcha biotite gabbro, Beleuti gabbro and Kalmakyr gabbro for Laser Ablation Inductively Coupled Plasma Mass Spectrometry (LA-ICP-MS) U—Pb dating. Reflected, transmitted light images in combination with the cathodoluminescence (CL) images were acquired to examine the internal structures before U—Pb dating. Zircon U—Pb dating was performed using LA-ICP-MS at the Continental Tectonics and Dynamics Laboratory of Institute of Geology, Chinese Academy of Geological Sciences, Beijing. A Finnigan Neptune MC-ICP-MS instrument was used for U-Th-Pb dating. The laser-ablation system was developed by the GeoLasPro 193 nm and established by the U. S. Coherent Co. Ltd. Helium was used as the carrier gas. Laser energy was 10 J/cm2 in energy density and 8 Hz in frequency. U and Pb of the zircon were ionized in plasma by hyperthermia up to 8000 °C. The analytical procedures included 4 s to determine the background and 23 s for each spot. The MC-ICP-MS operating conditions were optimized by the zircon standard 91,500, for maximum sensitivity, minimum oxide production rate (ThO + Th < 2%) and the lowest background. The accuracy of the data was monitored by GJ-1 as standard. The standard zircon 91,500 and one GJ-1 were analyzed for every 5 sample spots. The common Pb calibration is based on the method of Andersen (2002). The concordia diagrams and weighted mean calculation were made by Isoplot program (ver3.0; Ludwig, 2003).

4.3. Whole-rock major and trace elements analysis

Whole-rock major and trace elements were measured at the National Research Centre for Geoanalysis, Beijing. Major element analysis was conducted by XRF (X-ray fluorescence spectrometer) with Phillips PW4400 (XRF-1500) instrument. The uncertainties are better than 1% according to the standards GSR-3 (basalt) and GSR-2 (andesite). The loss on ignition (LOI) of the samples was calculated after heating at 980 °C for ~ 30 min. The FeO content was analyzed by the conventional wet chemical methods. Trace elements were analyzed by the PE300D ICP-MS. Two Chinese national standards (GSR-2 and GSR-3) were employed to monitor the accuracy, which is better than 5% for most trace elements in our study. Detailed description of the analyzed procedure was reported by Norrish and Chappell (1997) for major elements and Qi et al. (2000) for trace elements, respectively.

4.4. Zircon trace elements in situ

LA-ICP-MS analysis was conducted at the State Key Laboratory of Geological Processes and Mineral Resources, China University of Geosciences, Wuhan. Trace elements of the zircon grains were

measured in situ with an Element 2 Plasma Mass Spectrometer (Thermo-scientific, Germany) with a UP 213 laser ablation system (New Wave Research, USA). Detailed description of the analytical procedure was reported by Liu et al. (2008). A beam diameter of 40 μm was employed, with instrument setting as 10 Hz with pulse energy of 2 mJ per pulse, with 12 s background sampling followed by ca. 43 s data acquisition. The sampling system was purged for 15 s via helium gas. The total time of the ion signal collection is ca. 70 s. Residence time for ^{7}Li and ^{31}P is 5 ms, while that for the other element is 4 ms (a total measure time of 0.757 s). The low resolution mode was employed for trace element analysis. Data calibration was done by the ICPMSData software (Liu et al., 2010). Standards used to monitor the analytical procedure are Technology Standard Reference Material 612 (NIST 612, synthetic silicate melt glass) and National Institute of Standards.

4.5. Zircon Lu—Hf isotopes

Zircon Lu—Hf isotopic ratios were measured at the Continental Tectonics and Dynamics Laboratory of Institute of Geology, Chinese Academy of Geological Sciences, using a Neptune MC-ICP-MS with a Compex pro.193 nm UV laser ablation system. The laser ablation beam is 40 μm in diameter, and Helium was used as a carrier gas. The international reference zircon standard GJ-1 was used during the analytical procedure. The analytical spots are the same as those for U—Pb dating. Detailed description of the instruments conditions is given in Hou et al. (2007). $^{176}Yb/^{173}Yb = 0.796218$ and $^{176}Lu/^{175}Lu = 0.02658$ ratios were computed applying correction for isobaric interferences of ^{176}Lu and ^{176}Yb on ^{176}Hf (Chu et al., 2002). Additionally, for the instrumental mass bias correction, Yb isotopes were normalized to $^{172}Yb/^{173}Yb$ of 1.35274 by an exponential law, and Hf isotopes were normalized to $^{179}Hf/^{177}Hf$ of 0.7325 (Chu et al., 2002). The mass bias behavior of Lu is taken to be the same to Yb. The weighted mean $^{176}Hf/^{177}Hf$ value of 0.282013 ± 8 (2σ, n = 10) is in agreement with $^{176}Hf/^{177}Hf$ ratio (0.282013 ± 19 (2σ)) reported by Elhlou et al. (2006).

4.6. Whole-rock Rb—Sr and Sm—Nd isotopes

Sr and Nd isotopes were determined using by a *Neptune Plus MC-ICP-MS* with a 'wet' sample introduction system, at the State Key Laboratory of Geological Processes and Mineral Resources, China University of Geosciences, Beijing. The sample power (~50 mg) was dissolved in PFA beakers (Savillex®) using HF-HNO_3-HCl. The Sr and Nd were purified by passing the pre-cleaned Bio-Rad cation AG50W-X12 (200–400 mesh chloride form, USA) resin and LN resin in HCl. The mass fractionations for Sr and Nd isotope were calibrated by $^{86}Sr/^{88}Sr = 0.1194$ and $^{146}Nd/^{144}Nd = 0.7219$ based on the exponential law. The long-term reference value of NIST SRM 987 was $^{87}Sr/^{86}Sr = 0.7102631 \pm 20$ (2σ), and the value for Alfa Nd is $^{143}Nd/^{144}Nd = 0.512434 \pm 20$ (2σ). The $^{87}Sr/^{86}Sr$ and $^{143}Nd/^{144}Nd$ ratios of standard BHOV-2 in our study are 0.703469 ± 11 and 0.512986 ± 8, respectively, which agree with the reported data (Li et al., 2012 and references therein).

5. Results

5.1. Mineral chemistry

5.1.1. Feldspar

The results of feldspar analysis are listed in Supplementary Table A.1. Plagioclase is present in the Akcha biotite gabbro and Beleuti gabbro. In the Akcha biotite gabbro, plagioclase is mainly labradorite and andesine with a wide compositional range of $An_{35.90–68.17}Ab_{31.17–60.82}Or_{0.65–5.92}$, whereas that of the Beleuti gabbro is dominated by bytownite and anorthite ($An_{70.84–93.84}Ab_{6.05–21.63}Or_{0–7.73}$) as well as andesine ($An_{42.88–48.66}Ab_{50.57–56.62}Or_{0.50–0.77}$;Fig. 3a). Two profiles were analyzed by EMPA to check zoning in plagioclase. The results show that the plagioclase in Akcha biotite gabbro has a normal zoning with core of $An_{50.66–69.05}Ab_{30.35–47.75}Or_{0.60–1.59}$ and rim of $An_{45.20–46.8}Ab_{51.81–53.41}Or_{1.27–1.89}$, whereas plagioclase in the Beleuti gabbro shows an abrupt decrease of An from 82.49–91.00 to 44.36–46.22 (Fig. 3a).

5.1.2. Pyroxene

The compositions of pyroxene are presented in Supplementary Table A.2, and plotted into the classification diagram of wollastonite-enstatite-forsterite (Wo-En-Fs; Fig. 3b). The clinopyroxene in the Akcha biotite gabbro is dominated by augite with composition of $Wo_{42.31–42.42}En_{39.07–39.30}Fs_{16.30–17.12}$, and has $Mg^{\#}$ ($100 \times$ molar $Mg^{2+}/(Mg^{2+}+Fe^{2+})$) ranging from 70 to 75. Orthopyroxene in the Akcha biotite gabbro is clinoenstatite in composition. In the Beleuti gabbro, the pyroxene is mainly augite with a composition of $Wo_{46.36–48.59}En_{35.2–38.84}Fs_{12.89–16.13}$ and $Mg^{\#}$ values of 69–76. Compositions of the clinopyroxene in the Kalmakyr gabbro are $Wo_{25.85–27.19}En_{53.27–53.38}Fs_{17.67–18.50}$, and plot mostly in the pigeonite field in the Wo-En-Fs diagram, displaying low-Ca affinity. The $Mg^{\#}$ values of the pigeonite range from 75 to 76.

5.1.3. Biotite

Biotite occurs in the Akcha biotite gabbro and Kalmakyr gabbro, and show distinct chemical compositions (Supplementary Table A.3; Fig. 3c). The biotite in the gabbro is Fe-biotite, and characterized by low TiO_2 (2.25–4.51 wt%), MgO (6.07–13.61 wt%) and high FeO (16.00–25.44 wt%) contents with Mg/(total Fe + Mg) ratio of 0.30 to 0.60. The biotite in the Kalmakyr gabbro falls in the Mg-biotite field. In comparison, they show higher MgO (14.80–17.10 wt%), higher Mg/(total Fe + Mg) ratios (0.64–0.70) and lower FeO (13.06–16.59 wt%) and TiO_2 (2.17–3.33 wt%) contents with F concentration of 0.42–1.29 wt%.

5.1.4. Amphibole

According to the nomenclature of Leake et al. (1997), amphiboles in the Akcha biotite gabbro and Beleuti gabbro are all the calcic amphiboles (Supplementary Table A.4). Amphibole in the Beleuti gabbro displays large compositional range, varying from pargasite to edenite (Fig. 3d). They show large variations in Al_2O_3 (4.45–12.22 wt%), TiO_2 (0.37–2.41 wt%), FeO (11.62–16.53 wt%), MgO (11.02–14.06 wt%) and CaO (10.90–12.14 wt%). The $Mg^{\#}$ ranges from 0.56 to 0.75. Those in the Akcha gabbro are dominated by edenite and edenitic hornblende, with $Mg^{\#}$ values ranging from 0.58 to 0.65. Based on the empirical formula proposed by Ridolfi et al. (2010), the Akcha biotite gabbro yields oxygen fugacity of $\log fO_2 = -13.03$ to -13.8 and water contents of 4.9 to 5.3 wt%, whereas the Beleuti gabbro shows oxygen fugacity of $\log fO_2 = -10.1$ to -13.9 and water contents of 5.6 to 6.8 wt%.

5.2. Zircon U—Pb dating

The zircon grains from Akcha biotite gabbro show a size range of 70–150 μm with a width/length ratio of 1:1–1:3. In CL images most zircon grains exhibit oscillatory growth zoning, and their Th/U ratios vary from 0.84 to 2.28 (Table 1), typical of magmatic origin (Corfu et al., 2003; Koschek, 1993). Zircons with cores that are unzoned with strong luminescence are also recognized. The cores are ~20 to 40 μm in size, and are interpreted to represent inherited grains. Twenty-one of twenty-two analyses of zircon grains yield $^{206}Pb/^{238}U$ ages ranging from 334 to 348 Ma with a weighted mean $^{206}Pb/^{238}U$ ages of 339.9 ± 2.0Ma (MSWD = 0.70; Fig. 4a-b). One grain shows a $^{206}Pb/^{238}U$ age of 1702 Ma, which is inferred as inherited zircon.

The zircon grains from Beleuti gabbro are 50–100 μm long and exhibit width/length ratio of 1:1 to 1:2. Oscillatory zoning is also developed but not as clear as those in the Akcha biotite gabbro. Th/U ratios of these grains range from 0.62 to 1.61, indicating a magmatic origin (Table 1). Eleven of thirteen grains yield $^{206}Pb/^{238}U$ ages in the range of 332 to 348 Ma, with a weighted mean age of 339.0 ± 3.3 Ma

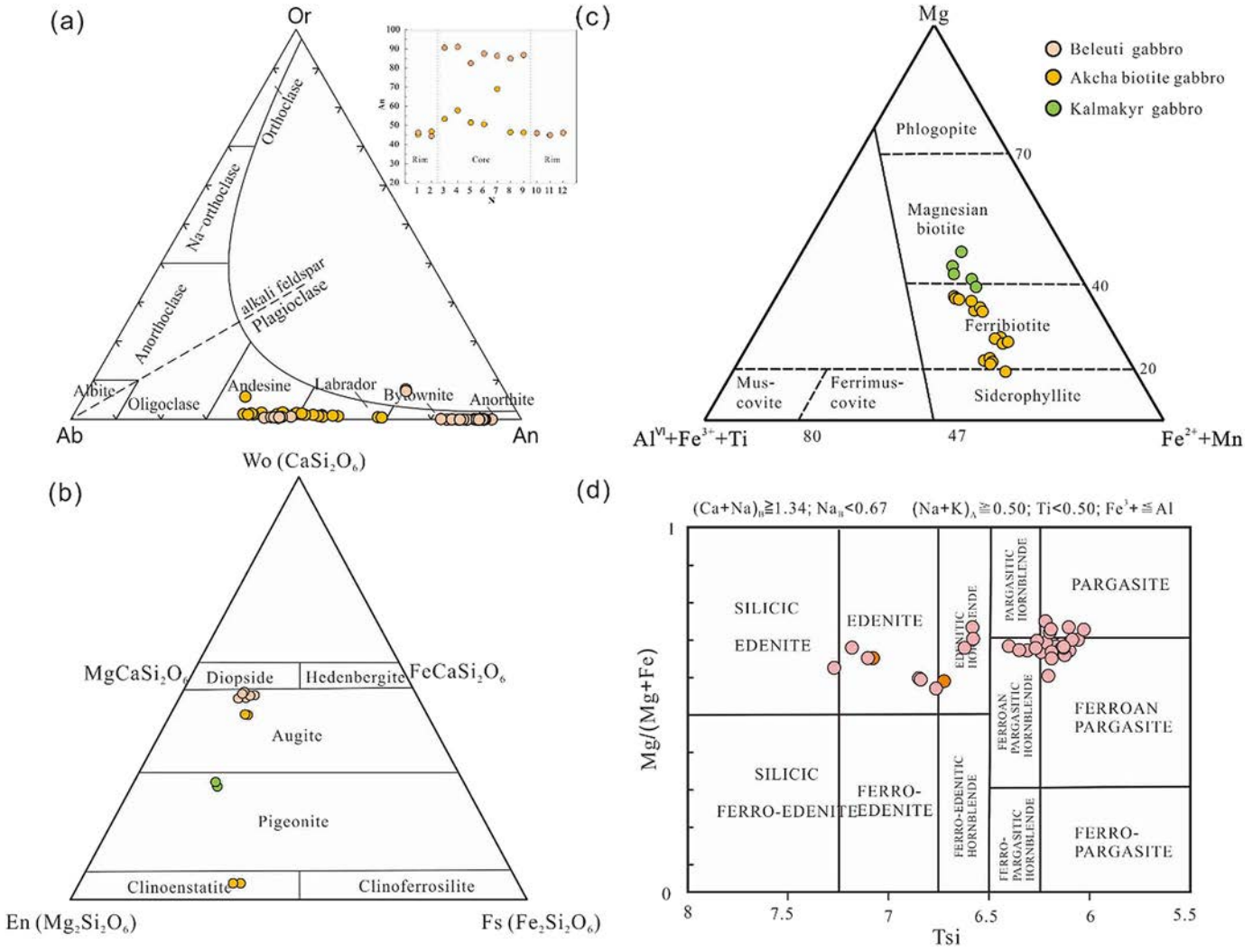

Fig. 3. (a) An-Ab-Or classification diagram of feldspar; (b) The En-Wo-Fs diagram of pyroxene; (c) The classification diagram of biotite (after Foster, 1960). (d) The classification diagram of amphibole (after Leake et al., 1997).

(MSWD = 0.76; Fig. 4c-d). Two grains yield $^{206}Pb/^{238}U$ ages of 436 and 1928 Ma, respectively, indicating inherited or entrained origin.

The Kalmakyr gabbro carries typical magmatic zircons with oscillatory zoning and Th/U ratios ranging from 0.52 to 0.79 (Table 1) with an average diameter of around 100 μm, and width/length ratios between 1:1.5 and 1:3. Fourteen grains display $^{206}Pb/^{238}U$ ages ranging from 329 to 345 Ma, with a weighted mean age of 335.0 ± 2.4 Ma (MSWD = 0.89; Fig. 4e-f).

5.3. Whole-rock major and trace elements

5.3.1. Major elements

Major and trace elements are presented in the Table 2. The Akcha biotite gabbro displays SiO_2 abundance ranging from 43.27 to 50.90 wt%, 18.58 to 21.67 wt% for Al_2O_3, 3.96 to 5.67 wt% for FeO, 3.35 to 4.53 wt % for Fe_2O_3, 7.71 to 10.72 wt% for CaO, 2.97 to 6.68 wt% for MgO, 1.37 to 3.26 wt% for Na_2O, 1.09 to 2.38 wt% for K_2O. Mg# (Mg# = Mg/[Mg + Fe^{2+}] × 100, mol %) values range from 41 to 56. Fe_2O_3/FeO ratios range from 0.78 to 0.91. Notably, the sample of chilled margin is characterized by the higher Mg# value (58), $Na_2O + K_2O$ contents (7.02 wt%), and lower Fe_2O_3/ FeO (0.60), CaO (4.82 wt%), Al_2O_3 (16.05 wt%), FeO (4.43 wt%) and Fe_2O_3 (2.65 wt%). In the diagram of SiO_2 vs. K_2O, most samples plot in the field of high-K calc-alkalic, and have A/CNK [Al_2O_3/($Na_2O + K_2O$-CaO)] values varying from 0.75 to 0.90, indicating metaluminous characteristics (Fig. 5).

The Beleuti gabbro exhibits SiO_2 from 41.60 to 46.96 wt%, Al_2O_3 from 16.37 to 20.08 wt%, Fe_2O_3 from 3.16 to 5.81 wt%, FeO from 4.84 to 6.95 wt%, MgO from 6.42 to 8.54 wt%, CaO from 9.55 to 16.06 wt%, Na_2O from 1.20 to 2.03 wt% and K_2O from 0.40 to 1.41 wt%. Mg# values are from 52 to 61, which are higher than those of the Akcha biotite gabbro. Compared to Akcha biotite gabbro, the Beleuti gabbro has similar Fe_2O_3/FeO ratios ranging from 0.60 to 0.92. As shown in the SiO_2 vs. K_2O plot, they fall into calc-alkalic and high-K calc-alkalic (Fig. 5a). The A/CNK values range from 0.50 to 0.89 (Fig. 5b).

The Kalmakyr gabbro shows SiO_2 abundance in the range of 44.12 to 45.58 wt%, 4.20 to 7.65 wt% for FeO, 3.85 to 6.55 wt% for Fe_2O_3, 5.52 to 7.4 wt% for MgO, 13.56 to 21.77 wt% for Al_2O_3, 3.29 to 7.36 wt% for CaO, 2.13 to 4.46 wt% for K_2O and 0.38 to 2.76 wt% for Na_2O. Their Mg# values display variation from 49 to 55. The samples are mainly plotted in the shoshonitic field (Fig. 5a). The Akcha biotite gabbro, Beleuti gabbro and Kalmakyr gabbro do not show any clear evolution trends in the Harker diagram (Fig. 6).

5.3.2. Trace elements

Trace elements data are listed in Table 2. The rocks have total rare earth element (REE) content varying from 13.5 to 123.0 ppm for Akcha biotite gabbro, 24.5 to 37.5 ppm for Beleuti gabbro and 27.1 to 70.4 ppm for Kalmakyr gabbro. Typically, they have slight Eu anomalies with Eu/Eu* values [Eu/($(Sm \times Gd)^{1/2}$)] of 0.73 to 1.59 for Akcha biotite gabbro, 0.95 to 1.23 for Beleuti gabbro and 1.24 to 1.51 for Kalmakyr

Table 1
The LA-ICP-MS zircon U–Pb ages for the gabbroic intrusions in the Valerianov-Beltau-Kurama magmatic arc, Uzbekistan.

Sample	Contents (ppm)				Isotopic ratios						Age (Ma)					
Akcha biotite gabbro																
AK-8	Pb	Th	U	Th/U	$^{207}Pb/^{206}Pb$	1s	$^{207}Pb/^{235}U$	1s	$^{206}Pb/^{238}U$	1s	$^{207}Pb/^{206}Pb$	1s	$^{207}Pb/^{235}U$	1s	$^{206}Pb/^{238}U$	1s
AK-8-01	68	163.9	173.6	0.9439	0.0521	0.0005	0.3890	0.0048	0.0542	0.0006	287.1	22.2	333.6	3.6	340.0	3.4
AK-8-02	45.4	106.6	120.8	0.8820	0.0529	0.0023	0.3991	0.0219	0.0546	0.0008	324.1	100.0	341.0	15.9	342.5	5.2
AK-8-03	213	521.4	455.5	1.1448	0.0522	0.0004	0.3891	0.0039	0.0541	0.0005	300.1	16.7	333.7	2.9	339.4	3.3
AK-8-06	121	295.4	216.1	1.3669	0.0519	0.0005	0.3937	0.0065	0.0550	0.0009	283.4	41.7	337.1	4.8	345.0	5.3
AK-8-08	113	282.3	195.1	1.4468	0.0522	0.0006	0.3893	0.0069	0.0540	0.0008	294.5	27.8	333.9	5.1	339.3	5.1
AK-8-09	50.9	120.6	125.6	0.9604	0.0521	0.0007	0.3984	0.0066	0.0554	0.0009	300.1	33.3	340.5	4.8	347.7	5.6
AK-8-10	74	179.5	163.2	1.0995	0.0521	0.0007	0.3957	0.0064	0.0550	0.0009	300.1	33.3	338.5	4.7	345.3	5.3
AK-8-11	4330	11,105.1	4865.2	2.2826	0.0538	0.0005	0.4018	0.0060	0.0542	0.0008	361.2	22.2	343.0	4.4	340.1	5.1
AK-8-12	210	528.7	334.7	1.5798	0.0549	0.0024	0.4066	0.0216	0.0536	0.0008	405.6	94.4	346.4	15.6	336.5	4.9
AK-8-13	58	141.8	169.3	0.8377	0.0519	0.0006	0.3826	0.0061	0.0535	0.0007	279.7	−69.4	329.0	4.6	335.8	4.3
AK-8-14	670	36.1	2270.3	0.0159	0.1260	0.0009	5.2528	0.0718	0.3022	0.0044	2042.9	13.0	1861.2	12.3	1702.2	22.0
AK-8-15	65	159.3	182.9	0.8708	0.0518	0.0006	0.3831	0.0061	0.0536	0.0007	276.0	−75.0	329.3	4.5	336.8	4.4
AK-8-16	91	225.3	176.4	1.2774	0.0522	0.0006	0.3850	0.0057	0.0535	0.0007	300.1	27.8	330.7	4.2	336.0	4.4
AK-8-17	197	482.7	334.1	1.4446	0.0524	0.0005	0.4007	0.0073	0.0554	0.0009	305.6	36.1	342.1	5.3	347.5	5.7
AK-8-18	1719	3294.8	2311.6	1.4253	0.0536	0.0004	0.4078	0.0115	0.0551	0.0015	353.8	16.7	347.3	8.3	346.0	9.1
AK-8-19	1122	2796.2	1543.4	1.8118	0.0527	0.0006	0.4001	0.0075	0.0550	0.0009	316.7	22.2	341.8	5.5	345.2	5.3
AK-8-20	48.6	118.8	128.7	0.9234	0.0526	0.0007	0.3920	0.0071	0.0540	0.0009	322.3	27.8	335.8	5.2	339.1	5.3
AK-8-21	55.3	132.4	148.0	0.8946	0.0518	0.0022	0.3867	0.0066	0.0542	0.0008	276.0	100.0	332.0	4.9	340.1	4.8
AK-8-22	77	179.5	186.0	0.9650	0.0544	0.0012	0.4113	0.0091	0.0548	0.0009	387.1	50.0	349.8	6.6	344.1	5.6
AK-8-25	195	497.7	306.0	1.6267	0.0530	0.0005	0.3888	0.0048	0.0532	0.0006	327.8	36.1	333.5	3.6	334.3	3.9
AK-8-26	63	158.6	159.7	0.9927	0.0525	0.0004	0.3852	0.0072	0.0532	0.0009	305.6	36.1	330.9	5.3	334.2	5.4
AK-8-27	55.5	137.4	109.0	1.2605	0.0521	0.0006	0.3900	0.0062	0.0542	0.0007	300.1	27.8	334.4	4.6	340.4	4.5
Beleuti gabbro																
BU-17	Pb	Th	U	Th/U	$^{207}Pb/^{206}Pb$	1s	$^{207}Pb/^{235}U$	1s	$^{206}Pb/^{238}U$	1s	$^{207}Pb/^{206}Pb$	1s	$^{207}Pb/^{235}U$	1s	$^{206}Pb/^{238}U$	1 s
BU-17-01	2062	3071.6	4719.1	0.6509	0.0612	0.0011	0.4631	0.0084	0.0550	0.0013	655.6	38.9	386.4	5.9	345.0	7.7
BU-17-03	1290	437.1	780.9	0.5598	0.1374	0.0013	6.6247	0.3020	0.3486	0.0131	2194.8	30.6	2062.6	40.4	1928.1	62.5
BU-17-04	487	324.4	1155.1	0.2809	0.0840	0.0036	0.8239	0.0751	0.0699	0.0035	1294.4	83.3	610.2	41.8	435.6	21.4
BU-17-05	816	1294.9	2095.4	0.6180	0.0669	0.0012	0.4881	0.0134	0.0528	0.0006	835.2	50.5	403.6	9.2	331.9	4.0
BU-17-06	650	1582.2	2224.3	0.7113	0.0530	0.0003	0.3974	0.0063	0.0544	0.0008	327.8	11.1	339.8	4.7	341.2	5.1
BU-17-09	1031	2575.8	2233.9	1.1530	0.0585	0.0007	0.4395	0.0136	0.0544	0.0013	546.3	41.7	369.9	9.6	341.8	7.9
BU-17-11	1204	2716.8	3672.9	0.7397	0.0579	0.0009	0.4349	0.0092	0.0546	0.0017	527.8	33.3	366.7	6.6	342.7	10.1
BU-17-13	2327	6188.3	4510.5	1.3720	0.0539	0.0003	0.4050	0.0073	0.0545	0.0009	368.6	11.1	345.2	5.3	341.9	5.8
BU-17-15	2329	6504.7	4434.4	1.4669	0.0538	0.0003	0.3957	0.0080	0.0533	0.0011	361.2	2.8	338.5	5.9	335.0	6.5
BU-17-16	2079	5542.6	3988.5	1.3897	0.0542	0.0003	0.4062	0.0067	0.0544	0.0009	388.9	11.1	346.2	4.9	341.2	5.3
BU-17-17	2446	6526.6	7408.0	0.8810	0.0550	0.0003	0.4055	0.0056	0.0535	0.0008	413.0	11.1	345.7	4.1	335.8	4.8
BU-17-18	5193	14,269.2	8839.5	1.6143	0.0553	0.0002	0.4112	0.0061	0.0540	0.0008	433.4	11.1	349.7	4.4	338.7	4.9
BU-17-21	2644	7741.6	4798.7	1.6133	0.0540	0.0002	0.4124	0.0071	0.0554	0.0010	368.6	11.1	350.6	5.1	347.8	6.0
Kalmakyr gabbro																
KLMK-1	Pb	Th	U	Th/U	$^{207}Pb/^{206}Pb$	1s	$^{207}Pb/^{235}U$	1 s	$^{206}Pb/^{238}U$	1s	$^{207}Pb/^{206}Pb$	1s	$^{207}Pb/^{235}U$	1s	$^{206}Pb/^{238}U$	1s
KLMK-1-01	284	698.7	916.8	0.7621	0.0524	0.0003	0.3836	0.0050	0.0531	0.0007	301.9	11.1	329.7	3.7	333.4	4.3
KLMK-1-02	112	253.2	468.7	0.5403	0.0534	0.0004	0.3967	0.0044	0.0539	0.0006	342.7	16.7	339.2	3.3	338.4	3.8
KLMK-1-03	102	238.7	389.5	0.6128	0.0540	0.0004	0.3902	0.0046	0.0524	0.0006	368.6	16.7	334.5	3.4	329.3	3.7
KLMK-1-04	194	461.9	745.2	0.6199	0.0523	0.0003	0.3792	0.0052	0.0525	0.0007	298.2	11.1	326.4	3.9	330.1	4.3
KLMK-1-05	375	816.4	1034.6	0.7891	0.0629	0.0004	0.4621	0.0057	0.0532	0.0007	705.6	11.1	385.7	4.1	334.4	4.3
KLMK-1-06	140	333.5	498.7	0.6688	0.0527	0.0004	0.3833	0.0053	0.0527	0.0007	316.7	−2.8	329.5	4.0	331.2	4.6
KLMK-1-07	143	330.1	571.9	0.5773	0.0525	0.0004	0.3869	0.0053	0.0534	0.0007	305.6	30.6	332.1	3.9	335.7	4.4
KLMK-1-08	187	441.7	646.6	0.6832	0.0535	0.0004	0.3911	0.0052	0.0530	0.0006	346.4	16.7	335.1	3.8	333.2	3.9
KLMK-1-09	164	385.0	615.3	0.6257	0.0523	0.0004	0.3904	0.0066	0.0541	0.0009	301.9	16.7	334.7	4.9	339.5	5.8
KLMK-1-11	145	335.0	640.5	0.5229	0.0523	0.0004	0.3858	0.0058	0.0535	0.0008	301.9	16.7	331.3	4.3	335.7	5.0
KLMK-1-13	248	593.3	841.9	0.7047	0.0525	0.0003	0.3909	0.0068	0.0540	0.0009	305.6	30.6	335.0	5.0	338.9	5.5
KLMK-1-16	257	553.4	823.0	0.6724	0.0601	0.0024	0.4443	0.0243	0.0534	0.0009	605.6	88.9	373.3	17.1	335.6	5.8
KLMK-1-18	185	437.1	654.2	0.6681	0.0524	0.0003	0.3951	0.0074	0.0546	0.0010	305.6	16.7	338.1	5.5	343.0	6.3
KLMK-1-20	252	564.4	809.9	0.6968	0.0555	0.0004	0.4202	0.0074	0.0549	0.0009	431.5	2.8	356.2	5.3	344.7	5.3

gabbro, respectively. All the samples show similar chondrite-normalized REE patterns, which are characterized by slight enrichment in light rare earth elements (LREEs) and low heavy rare earth elements (HREE) with low $(La/Yb)_N$ ratios ranging from 2.00 to 13.01 (Fig. 7). The samples show significant enrichment in large-ion lithophile elements (LILEs) and low concentrations of high field strength elements (HFSEs). In the primitive mantle-normalized trace element spidergrams, they mostly show positive anomalies in Rb, Th, and strong negative anomalies of Nb, Ta, Zr, Hf and Ti (Fig. 7).

5.4. Zircon trace elements in situ

The zircon trace element data are listed in Table 3. All analyzed zircons are enriched in HREE relative to LREE, with positive Ce and negative Pr, Nd anomalies, which are typical characteristics of zircon in igneous rocks (Hoskin and Schaltegger, 2003). The Ce/Nd values for the Akcha, Beleuti and Kalmakyr gabbroic rocks show a range of 2.4–13.8 (avg. 6.7), 2.1–32.1 (avg. 7.2) and 4.8–15.9 (avg. 9.0), respectively. Based on the method suggested by Ballard et al. (2002), zircon

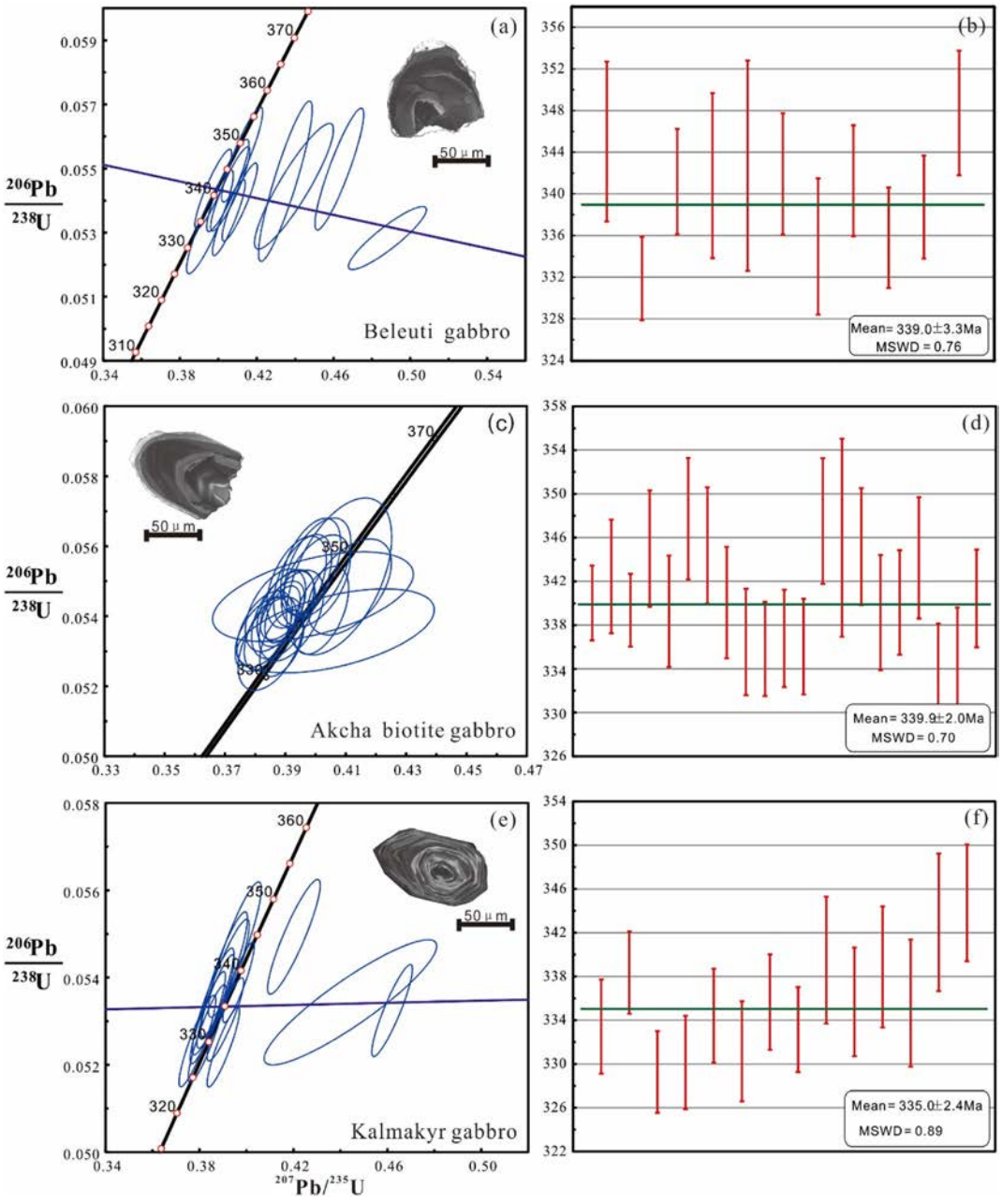

Fig. 4. Concordia diagram and weighted mean $^{206}Pb/^{238}U$ age for Beleuti gabbro (a-b), Akcha biotite gabbro (c-d) and Kalmakyr gabbro (e-f).

Ce^{4+}/Ce^{3+} ratios range from 14 to 179 (avg. 74, $n = 10$) for Akcha biotite gabbro, 17 to 268 (avg. 71, $n = 8$) for Beleuti gabbro and 77 to 220 (avg. 141, $n = 7$) for Kalmakyr gabbro. The oxygen fugacity ranges from −10.2 to −20.6 for Akcha biotite gabbro, −7.8 to −20.4 for Beleuti gabbro and − 15.8 to −18.2 for Kalmakyr gabbro. In the plot of $10^4/T$ vs. Ce^{4+}/Ce^{3+}, most of the samples fall in the field between the magnetite-hematite (MH) buffer and fayalite-magnetite-quartz (FMQ) buffer curve, which are lower than the porphyries from the giant porphyry deposits in the Central Asian Orogenic Belt (Fig. 8a).

5.5. Zircon Lu—Hf isotopes

The zircon Lu—Hf isotope data are listed in Table 4 and shown in Fig. 9a. The zircons in Akcha biotite gabbro with crystallization ages ranging from 334 to 348 Ma have positive $\varepsilon_{Hf(t)}$ values from 6.76 to 9.96. The single-stage Hf model ages (T_{DM}) are 589-707 Ma. The xenocryst zircon yields $\varepsilon_{Hf(t)}$ value of −11.21, with T_{DM} of 2549 Ma. The Beleuti gabbro shows Hf isotopic compositions with $\varepsilon_{Hf(t)}$ values of 3.38 to 7.01 and T_{DM} values of 732-837 Ma, respectively. The entrained zircons with ages of 436 and 1928 Ma display $\varepsilon_{Hf(t)}$ values of 6.57 and − 6.27 and T_{DM} values of 796 and 2563 Ma. In addition, zircons from Kalmakyr gabbro yield Hf isotopic compositions with $\varepsilon_{Hf(t)}$ values of 3.96 to 8.25 and T_{DM} values of 637-830 Ma.

In summary, zircons in the gabbroic intrusions display similar positive $\varepsilon_{Hf(t)}$ values ranging from 3.38 to 9.96. The younger entrained grain with an age of 436 Ma has positive $\varepsilon_{Hf(t)}$ value (6.57), whereas the older zircons with ages of 1702–1928 Ma show negative values of −11.21 to −6.27.

5.6. Whole-rock Rb—Sr and Sm—Nd isotopes

Rb—Sr and Sm—Nd isotopic compositions are reported in the Table 5 and shown in Fig. 9b, where the data are plotted in combination with those on porphyries from the giant porphyry deposits in Central Asia

Table 2
The major (wt%) and trace elements (ppm) for the gabbroic intrusions in the Valerianov-Beltau-Kurama magmatic arc, Uzbekistan.

No.	BU-10	BU-1	BU-5	BU-12	BU-14	BU-8	BU-9	BU-15	AK-13
Sample	Beleuti gabbro								Akcha
SiO_2	46.96	41.6	46.9	46.1	42.93	44.31	43.57	42.14	43.27
TiO_2	0.62	0.62	0.56	0.67	0.66	0.64	0.84	0.57	0.67
Al_2O_3	16.37	18.06	17.01	17.13	19.12	20.08	18.49	19.77	19.33
Fe_2O_3	3.16	5.81	3.21	3.82	5.61	4.36	5.39	4.96	4.40
FeO	5.25	6.76	4.84	5.30	6.95	6.53	5.85	6.65	5.67
MnO	0.16	0.17	0.15	0.15	0.18	0.16	0.14	0.16	0.21
MgO	6.73	8.54	6.82	6.62	7.76	6.80	6.42	8.54	6.68
CaO	16.06	11.88	15.27	15.77	12.14	9.55	13.33	12.21	10.72
Na_2O	1.82	1.35	2.03	1.61	1.26	2.20	1.20	1.17	1.37
K_2O	0.40	0.89	0.55	0.52	0.44	1.36	1.41	0.44	2.38
P_2O_5	0.12	0.04	0.11	0.10	0.03	0.12	0.05	0.06	0.01
LOI	2.12	3.15	2.27	1.78	1.44	2.53	2.01	1.74	3.72
Rb	8.03	23.2	11.1	11.3	8.55	38	43	8.91	98.1
Sr	639	509	671	629	660	660	555	672	419
Ba	196	296	216	188	194	566	589	227	752
Th	1.43	0.65	1.05	0.69	1.24	1.49	0.73	1.08	0.10
U	0.52	0.24	0.36	0.28	0.41	0.48	0.23	0.34	0.05
Nb	0.79	0.87	0.92	0.90	1.31	1.44	0.87	0.89	0.23
Ta	0.13	0.12	0.12	0.13	0.16	0.16	0.12	0.12	0.07
Zr	21.3	14.8	18.7	18.3	19.7	21.7	15.2	16	5.65
Hf	0.88	0.58	0.84	0.82	0.75	0.89	0.67	0.58	0.26
Cr	1.47	28.5	6.70	2.04	20.1	18.2	34.4	23.6	69.7
Pb	16.1	14.4	12.9	12.6	13.5	12.7	11.7	10.1	5.39
Cu	24.7	194	21.7	54.4	40	7.90	31.6	69.2	28.3
Ga	15.4	16.1	15.4	15.8	17.4	17.3	17.3	16.8	16.7
V	324	440	330	357	468	380	528	402	405
Cs	0.64	1.71	0.77	1.02	1.10	2.44	5.43	0.85	8.94
Cd	0.16	0.10	0.16	0.22	0.23	0.1	0.12	0.15	0.06
W	0.84	0.47	0.68	0.62	0.5	0.39	0.61	0.49	0.36
Mo	0.22	0.11	0.11	0.16	0.15	0.06	0.15	0.19	0.05
Cr	1.47	28.5	6.70	2.04	20.1	18.2	34.4	23.6	69.7
La	5.56	3.90	5.69	5.26	4.71	6.59	3.98	4.46	1.59
Ce	11.50	8.11	11.9	11.4	9.88	13.2	8.64	8.62	3.40
Pr	1.59	1.11	1.65	1.61	1.36	1.71	1.29	1.09	0.51
Nd	8.13	5.30	8.04	8.03	6.52	7.79	6.78	4.99	2.88
Sm	2.04	1.19	1.90	2.00	1.46	1.75	1.78	1.10	0.84
Eu	0.68	0.48	0.65	0.72	0.52	0.62	0.66	0.46	0.47
Gd	2.35	1.31	2.18	2.23	1.49	1.73	1.99	1.18	0.97
Tb	0.36	0.20	0.33	0.34	0.23	0.26	0.30	0.18	0.17
Dy	2.07	1.15	1.94	1.98	1.32	1.51	1.78	1.05	1.05
Ho	0.41	0.24	0.38	0.40	0.27	0.31	0.35	0.20	0.21
Er	1.19	0.67	1.11	1.17	0.81	0.93	1.01	0.60	0.63
Tm	0.15	0.09	0.14	0.15	0.11	0.12	0.13	0.08	0.08
Yb	1.00	0.62	0.95	0.99	0.76	0.85	0.85	0.55	0.57
Lu	0.15	0.09	0.15	0.15	0.11	0.13	0.13	0.08	0.09
Y	10.7	6.33	9.92	10.4	7.42	8.37	9.39	5.49	5.57

No.	AK-8	AK-5	AK-7	AK-6	AK-10	km-2	km-9	km-10
Sample	Akcha biotite gabbro					Kalmakyr gabbro		
SiO_2	50.89	54.89	50.8	49.26	47.16	45.46	45.58	44.12
TiO_2	0.96	1.12	1.00	1.23	0.73	0.38	0.70	0.70
Al_2O_3	18.66	16.05	19	18.58	21.67	13.56	20.7	21.77
Fe_2O_3	3.86	2.65	3.35	4.53	3.62	3.85	6.55	6.55
FeO	4.35	4.43	4.17	5.45	3.96	7.65	4.20	5.50
MnO	0.15	0.24	0.12	0.15	0.11	0.40	0.20	0.22
MgO	3.02	5.22	2.97	3.61	3.75	7.40	5.52	6.00
CaO	8.05	4.82	7.71	10.3	10.27	5.33	7.36	3.29
Na_2O	3.23	4.57	3.26	2.89	3.13	0.38	2.76	1.90
K_2O	1.82	2.45	1.58	1.09	1.59	2.46	2.13	4.46
P_2O_5	0.28	0.24	0.29	0.25	0.10	0.06	0.28	0.28
LOI	3.51	1.86	4.33	1.14	3.01	6.81	3.54	4.48
Rb	50.7	137	50.6	34.4	52.7	114	90.4	202
Sr	493	181	518	515	657	233	703	437
Ba	602	395	433	190	369	315	189	347
Th	3.43	5.21	4.45	3.52	1.22	1.12	0.67	0.72
U	0.83	1.25	1.16	0.99	0.3	0.38	0.3	0.29
Nb	5.37	8.19	5.07	5.72	1.73	1.32	1.04	0.86
Ta	0.37	0.59	0.42	0.5	0.14	0.16	0.12	0.09
Zr	82	172	75.3	34.4	25.4	14.9	8.82	6.18
Hf	2.67	4.73	2.49	1.41	0.88	0.48	0.30	0.24
Cr	19.3	103	17.8	8.28	7.46	11.6	11.2	11.7
Pb	12.8	3.28	7.90	4.10	17.7	77.2	42.4	9.68

(continued on next page)

Table 2 (*continued*)

No.	AK-8	AK-5	AK-7	AK-6	AK-10	km-2	km-9	km-10
Sample	Akcha biotite gabbro					Kalmakyr gabbro		
Cu	76.7	3.77	278	131	10.7	21,040	1054	1504
Ga	19.6	20	20	20.3	19.3	13.2	22.6	24.5
V	282	164	215	481	370	156	261	272
Cs	3.24	5.54	7.61	1.99	7.29	6.66	3.66	9.2
Cd	0.05	0.05	0.05	0.08	0.16	1.67	1.72	0.05
W	0.64	0.67	0.75	0.58	0.2	14.9	0.59	1.00
Mo	0.51	0.52	0.68	0.97	0.18	3.17	1.26	0.63
Cr	19.3	103	17.8	8.28	7.46	11.6	11.2	11.7
La	19.3	21.4	20.8	14.7	7.41	5.30	14.2	10.7
Ce	39.2	44.6	42.6	32.8	14.9	9.84	27	20.8
Pr	5.14	5.78	5.59	4.38	1.94	1.10	2.99	2.28
Nd	23.4	26	25.9	20.1	9.14	4.74	13.9	10.7
Sm	4.64	5.20	5.01	4.33	1.86	1.30	2.88	2.17
Eu	1.32	1.42	1.38	1.05	0.79	0.53	1.26	1.03
Gd	4.61	5.27	4.88	4.45	1.93	1.31	2.86	2.01
Tb	0.71	0.82	0.74	0.69	0.30	0.19	0.38	0.26
Dy	4.15	4.88	4.31	3.99	1.76	1.09	2.12	1.37
Ho	0.83	1.00	0.89	0.80	0.36	0.23	0.40	0.25
Er	2.47	3.03	2.64	2.36	1.07	0.70	1.18	0.75
Tm	0.33	0.40	0.34	0.31	0.14	0.10	0.15	0.10
Yb	2.22	2.78	2.31	1.98	0.93	0.62	0.93	0.59
Lu	0.34	0.41	0.35	0.30	0.14	0.09	0.14	0.08
Y	22.8	27.6	23.4	21.4	9.95	4.75	9.75	6.06

Orogenic Belt. The Akcha biotite gabbro shows $(^{87}Sr/^{86}Sr)_i$ ranging from 0.7051 to 0.7054 and ε_{Nd} values ranging from 0.14 to 1.68, whereas the sample of chilled margin has $(^{87}Sr/^{86}Sr)_i$ of 0.7065 and ε_{Nd} value of 1.96. The Beleuti gabbro shows uniform $(^{87}Sr/^{86}Sr)_i$ ranging from 0.7054 to 0.7057 and ε_{Nd} values around 0.90. The Kalmakyr gabbro yields initial $^{87}Sr/^{86}Sr$ ratios from 0.7044 to 0.7056 and ε_{Nd} values from 0.49 to −1.59. In comparison with the porphyries from the Kalmakyr and Sarycheku in the Almalyk orefield, these mafic intrusions show lower $(^{87}Sr/^{86}Sr)_i$ and higher ε_{Nd} values (Fig. 9b).

6. Discussion

6.1. Assessment of hydrothermal alteration and crustal contamination

The LOI of the rocks analyzed in this study ranges from 1.14 to 4.33 wt% for Akcha biotite gabbro, 1.44 to 3.15 wt% for Beleuti gabbro and 3.54 to 6.81 wt% for Kalmakyr gabbro, respectively. Petrographic observation confirmed that samples of Beleuti gabbro are fresh with no effects of alteration. However, the Kalmakyr gabbro and some of the Akcha biotite gabbro samples with high LOI values (up to 4.33 wt %) underwent hydrothermal alteration to some extent, which is also reflected by partial alteration to clay, carbonate and chlorite. As the immobile elements (e.g. REE and HFSE) are largely insensitive to post-magmatic alteration, we consider these elements to evaluate the petrogenesis of the rocks.

It is essential to assess the effects of crustal contamination before employing the geochemical data to trace the nature of mantle source. Crustal contamination is a common process for mafic-ultramafic intrusions during magma ascent from mantle source and the evolution in the crustal magma chamber (McBirney and Creaser, 2003; Namur et al., 2010). The presence of minor inherited zircons with ages of ca. 1702 Ma in Akcha biotite gabbro, and 436 Ma, 1928 Ma in Beleuti gabbro indicates that the magma witnessed crustal contamination to some extent. The two groups of plagioclase and the abrupt decrease of An in zoned plagioclase suggest that magma mixing might have occurred between mafic magma and more silicic crustal magma. The distinct Hf concentration in mafic intrusions (~0.2 ppm) and crust (up to 5.3 ppm) make the Hf isotopic composition a sensitive proxy to identify

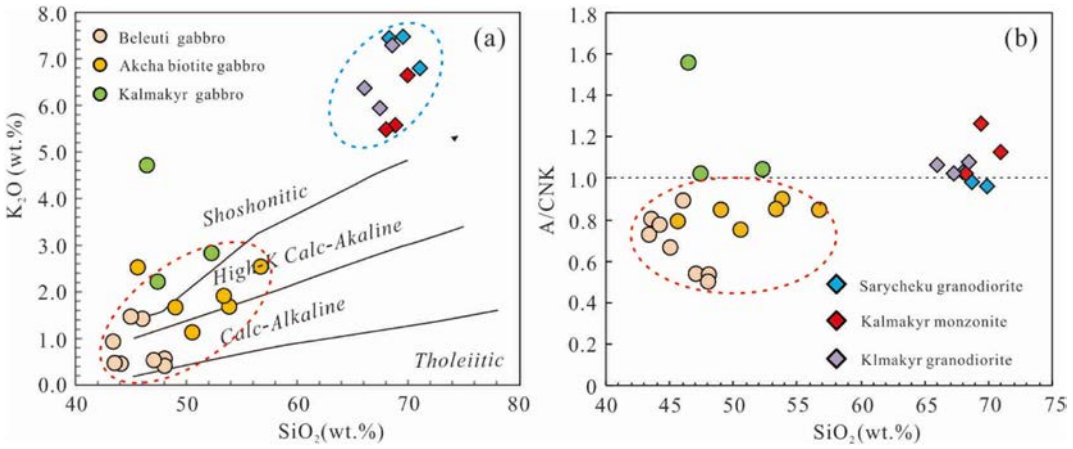

Fig. 5. (a) K_2O vs. SiO_2 diagram (Peccerillo and Taylor, 1976); (b) A/CNK vs. SiO_2 plots. Data source: ore-bearing porphyries from Sarycheku (granodiorite) and Kalmakyr (granodiorite and monzonite) deposits are from Cheng et al. (2018).

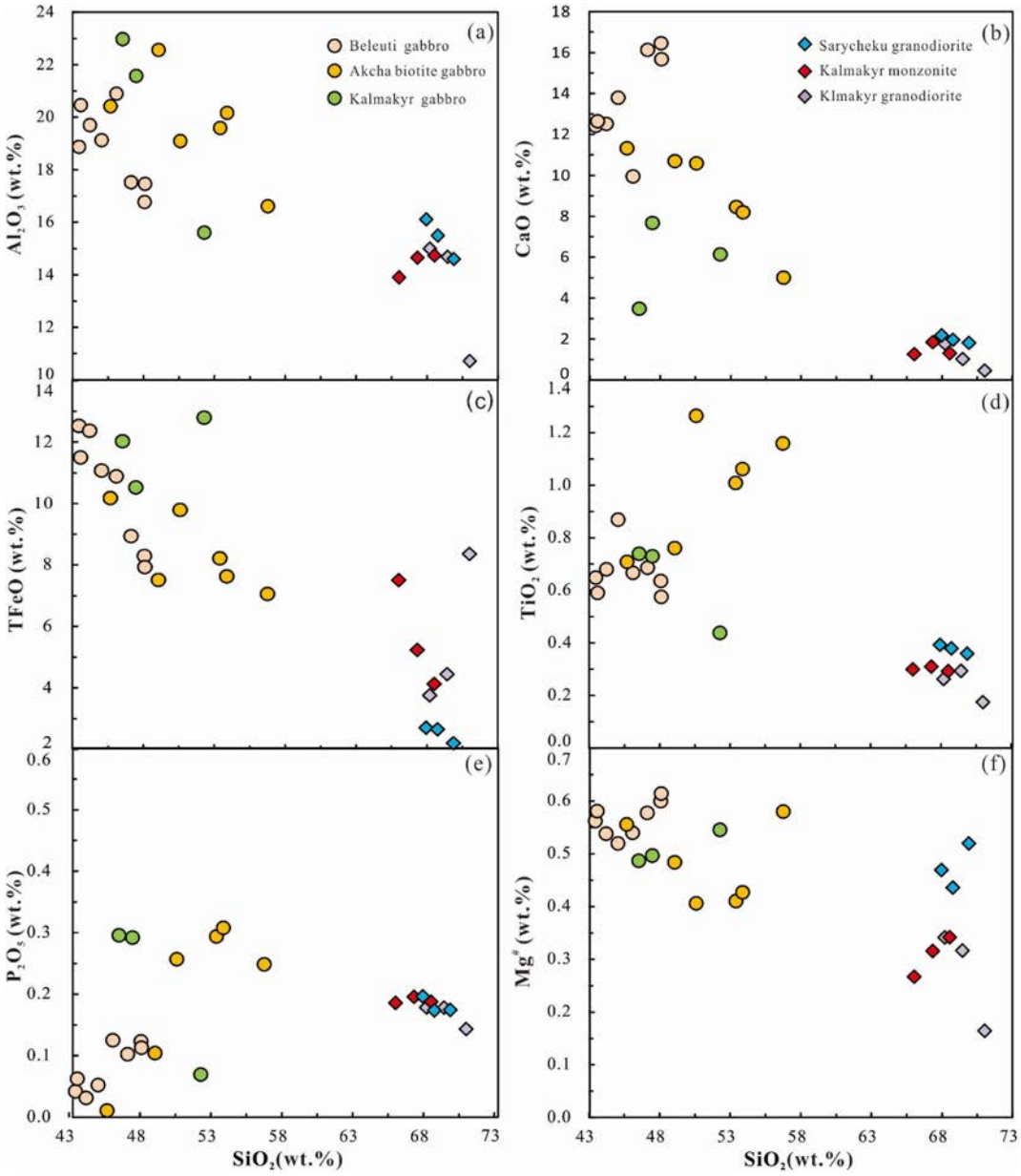

Fig. 6. Harker diagrams for gabbroic intrusions, together with the ore-related porphyries in Kalmakyr and Sarycheku deposits. Data source: ore-bearing porphyries from Sarycheku (granodiorite) and Kalmakyr (granodiorite and monzonite) deposits are from Cheng et al. (2018).

crustal contamination (Salters and Stracke, 2004). However, our samples generally show limited $\varepsilon_{Hf(t)}$ variations, e.g. 6.76–9.96 for Akcha biotite gabbro and 3.38–7.01 for Beleuti gabbro. Moreover, compared to the sample from the chilled margin ($(^{87}Sr/^{86}Sr)_i = 0.7065$), which is might have experienced higher degree of crustal contamination, the Sr isotopic signatures of Akcha biotite gabbro ($(^{87}Sr/^{86}Sr)_i = 0.7051$–$0.7054$) and Beleuti gabbro ($(^{87}Sr/^{86}Sr)_i = 0.7054$ to 0.7057) are homogeneous, and more depleted. Hence, the crustal contamination in Akcha biotite gabbro and Beleuti gabbro is inferred to be insignificant. On the other hand, the Kalmakyr gabbro displays a relatively wider range of $\varepsilon_{Hf(t)}$ (3.96–8.25), suggesting that the effect of crustal contamination was pronounced.

6.2. Petrogenesis of the gabbroic intrusions

Gabbroic intrusions in the Valerianov-Beltau-Kurama arc belt were formed synchronously (ca. 340 Ma) as indicated by the LA-ICP-MS zircon U—Pb age data. Even though they show similar geochemistry, there is no clear evolution trend in the Harker diagram from the Akcha biotite gabbro, Beleuti gabbro to Kalmakyr gabbro, precluding the possibility that they were generated from a single parental magma by fractional crystallization. In the diagram of La/Sm-La and Ce/Yb-Ce, Akcha biotite gabbro, Beleuti gabbro and Kalmakyr gabbro appear to be generated by different degrees of partial melting of a common metasomatized asthenosphere source instead of a co-magmatic evolution (Fig. 10).

As stated above, the gabbroic intrusions are characterized by LILE enrichment coupled with negative anomalies in HFSE, indicating a subduction-related affinity (Altherr et al., 2008; Boari et al., 2009; Briqueu et al., 1984). Based on the previous studies, the Valerianov-Beltau-Kurama arc is an Andean-type continental arc, where possible components in the magma source include 1) mantle wedge, 2) fluids released from subducted oceanic crust, 3) subducted sediments, and 4) melts derived from subducted oceanic crust (e.g. Cheng et al., 2018; Elburg et al., 2002; MacDonald et al., 2000; Muir et al., 1995; Seltmann et al., 2014; Zhao et al., 2015). However, the gabbroic intrusions in our study show

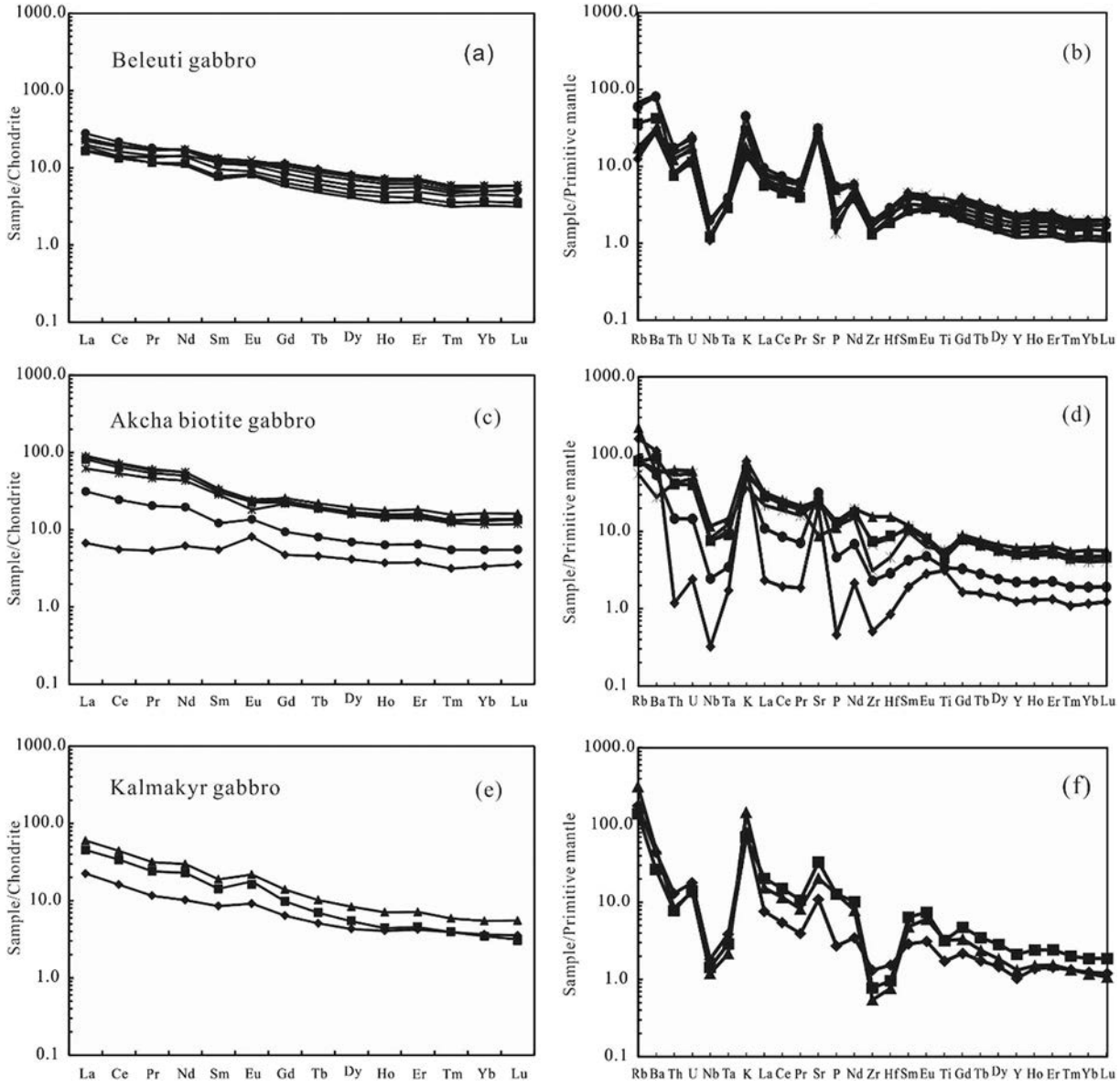

Fig. 7. Chondrite-normalized REE and primitive mantle-normalized trace element patterns of the gabbroic rocks. The Europium anomalous depends on the variation of the plagioclase content. (a-b) Beleuti gabbro; (c-d) Akcha biotite gabbro; (e-f) Kalmakyr gabbro. Primitive mantle and chondrite values are from Sun and McDonough (1989) and McDonough and Sun (1995), respectively.

Table 3
The zircon trace elements in situ for the gabbroic intrusions in the Valerianov-Beltau-Kurama magmatic arc, Uzbekistan.

Sample	La	Ce	Pr	Nd	Sm	Eu	Gd	Tb	Dy	Ho	Er	Tm	Yb	Lu
Beleuti gabbro														
BU-17-1	0.12	0.61	0.03	0.09	0.11	0.19	0.53	0.31	2.17	1.02	4.15	1.18	10.38	2.64
BU-17-2	0.06	0.62	0.02	0.14	0.29	0.32	0.95	0.47	2.88	1.21	4.59	1.26	10.39	2.51
BU-17-3	0.14	0.40	0.04	0.15	0.09	0.12	0.28	0.14	0.97	0.47	2.07	0.66	6.42	1.80
BU-17-4	0.01	0.86	0.01	0.03	0.05	0.03	0.15	0.08	0.51	0.22	0.87	0.24	2.04	0.46
BU-17-5	0.27	1.03	0.11	0.44	0.37	0.50	1.06	0.53	3.25	1.50	5.66	1.72	13.53	3.65
BU-17-6	0.05	0.57	0.02	0.13	0.19	0.31	0.76	0.42	2.51	1.24	4.66	1.56	12.21	3.71
BU-17-8	0.13	2.12	0.11	0.74	1.58	1.57	4.78	2.53	12.92	6.10	18.84	6.25	37.03	11.63
BU-17-9	0.34	1.86	0.22	0.89	0.93	1.49	2.76	1.51	8.17	4.47	13.75	4.56	23.74	7.35
Akcha biotite gabbro														
AK-8-1	0.00	0.35	0.00	0.05	0.14	0.07	0.62	0.37	2.49	1.23	4.95	1.37	10.80	2.62
AK-8-2	0.00	0.14	0.00	0.01	0.04	0.02	0.18	0.11	0.76	0.37	1.49	0.42	3.34	0.80
AK-8-3	0.00	0.16	0.00	0.02	0.06	0.03	0.31	0.17	1.15	0.55	2.20	0.60	4.66	1.13
AK-8-4	0.00	0.22	0.00	0.03	0.12	0.05	0.51	0.26	1.66	0.76	2.86	0.74	5.52	1.24
AK-8-5	0.00	0.15	0.00	0.02	0.04	0.03	0.20	0.12	0.85	0.41	1.68	0.48	3.71	0.91
AK-8-6	0.00	0.18	0.00	0.02	0.08	0.03	0.34	0.19	1.32	0.60	2.42	0.64	5.02	1.18

Table 3 (*continued*)

Sample	La	Ce	Pr	Nd	Sm	Eu	Gd	Tb	Dy	Ho	Er	Tm	Yb	Lu
AK-8-7	0.00	0.21	0.00	0.05	0.15	0.05	0.61	0.30	2.06	0.93	3.49	0.87	6.39	1.41
AK-8-8	0.00	0.26	0.01	0.07	0.16	0.05	0.70	0.37	2.49	1.14	4.52	1.15	8.92	2.11
AK-8-9	0.00	0.57	0.02	0.24	0.55	0.17	2.06	0.97	6.03	2.49	8.92	2.13	15.40	3.37
AK-8-10	0.00	0.30	0.01	0.11	0.25	0.08	1.12	0.57	3.58	1.57	5.77	1.39	10.10	2.24
Kalmakyr gabbro														
KLMK-1-1	0.02	15.16	0.05	0.95	2.67	0.74	15.93	5.12	54.71	21.62	101.63	23.57	241.10	52.59
KLMK-1-2	0.05	19.59	0.10	1.70	3.88	1.06	19.00	6.40	71.50	28.90	136.25	32.78	329.12	71.50
KLMK-1-3	0.05	18.67	0.14	2.29	4.14	1.35	20.24	6.96	81.35	33.79	163.28	39.27	399.28	89.45
KLMK-1-4	0.06	23.22	0.12	2.42	4.81	1.49	24.32	8.28	98.86	41.21	192.50	46.18	458.67	103.74
KLMK-1-5	0.33	21.96	0.37	3.46	3.13	0.94	15.50	5.05	60.67	25.88	123.68	30.43	308.61	69.86
KLMK-1-6	3.20	29.55	1.46	6.17	4.68	1.12	23.06	7.56	87.67	35.03	158.68	37.81	366.72	80.42
KLMK-1-8	1.85	30.86	0.59	4.50	4.93	1.36	26.25	8.72	99.03	40.25	183.36	43.50	423.18	92.07

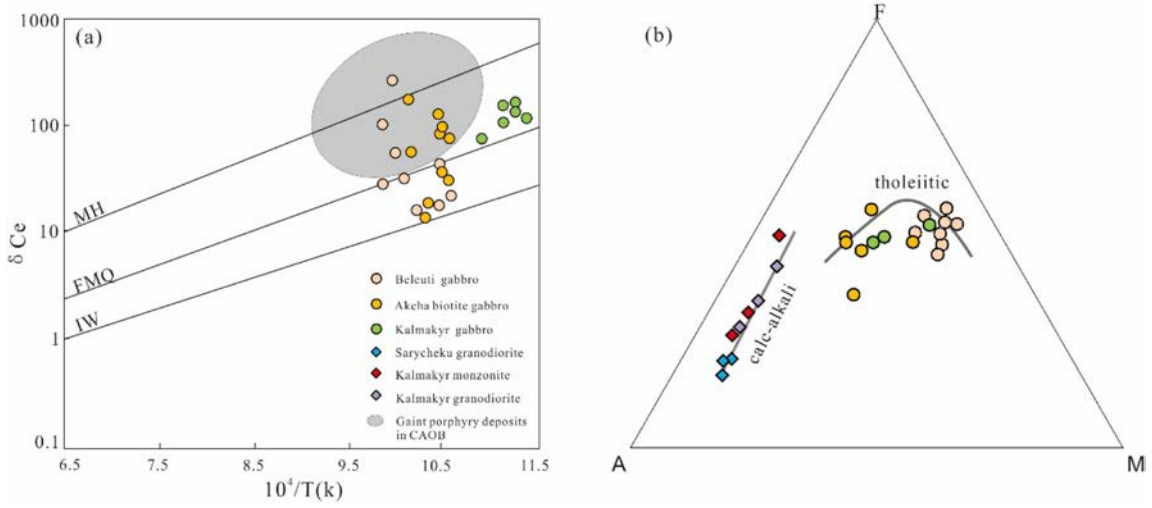

Fig. 8. (a) Comparison of the oxygen fugacity between the gabbroic rocks and ore-bearing porphyries in the CAOB; Data source: oxygen fugacity of the ore-bearing porphyries in the CAOB is from Shen et al. (2015) and Wu et al. (2015); (b) AFM diagram to show the evolution trends of the gabbroic rocks and porphyries of the Almalyk orefield. Data source: ore-bearing porphyries from Sarycheku (granodiorite) and Kalmakyr (granodiorite and monzonite) deposits are from Cheng et al. (2018).

Table 4
The zircon Hf isotopes for the gabbroic intrusions in the Valerianov-Beltau-Kurama magmatic arc, Uzbekistan.

Sample	Isotopic ratios						Corrected age			
Akcha biotite gabbro	$^{176}Yb/^{177}Hf$(corr)	2σ	$^{176}Lu/^{177}Hf$(corr)	2σ	$^{176}Hf/^{177}Hf$(corr)	2σ	Age	eHf(t)	TDM1 (Ma)	TDM2(Ma)
AK-8-02	0.027686	0.000276	0.000669	0.000003	0.282779	0.000016	343	7.64	664.50	861.41
AK-8-05	0.029342	0.000210	0.000774	0.000015	0.282779	0.000017	339	7.34	666.15	870.53
AK-8-06	0.053183	0.000866	0.001327	0.000014	0.282820	0.000018	345	8.98	618.10	777.68
AK-8-09	0.019322	0.000089	0.000495	0.000000	0.282767	0.000015	348	7.36	678.41	883.24
AK-8-10	0.025256	0.000168	0.000645	0.000001	0.282802	0.000013	345	8.52	631.27	806.89
AK-8-12	0.055793	0.000775	0.001467	0.000043	0.282805	0.000017	337	8.25	641.59	817.76
AK-8-14	0.011815	0.000064	0.000354	0.000001	0.281396	0.000015	1702	−11.21	2548.70	3078.67
AK-8-15	0.026229	0.000631	0.000719	0.000025	0.282787	0.000016	337	7.79	653.80	847.16
AK-8-17	0.040423	0.000037	0.001021	0.000005	0.282753	0.000015	348	6.76	707.08	921.60
AK-8-19	0.113091	0.000991	0.002925	0.000011	0.282858	0.000023	345	9.96	588.91	714.77
AK-8-20	0.018835	0.000205	0.000514	0.000007	0.282804	0.000016	339	8.46	627.49	806.09
AK-8-22	0.033759	0.000380	0.000858	0.000009	0.282784	0.000017	344	7.80	660.74	852.18
AK-8-24	0.035346	0.000358	0.000977	0.000006	0.282809	0.000017	339	8.35	626.96	805.53
AK-8-26	0.023378	0.000140	0.000619	0.000001	0.282821	0.000017	334	8.96	604.35	770.50
AK-8-28	0.025448	0.000757	0.000642	0.000015	0.282765	0.000018	339	7.28	683.94	889.47
Beleuti gabbro										
BU-17-03	0.033603	0.000165	0.000866	0.000006	0.281410	0.000017	1928	−6.27	2563.00	2946.56
BU-17-04	0.057682	0.001047	0.001709	0.000023	0.282701	0.000024	436	6.57	795.97	1001.00
BU-17-05	0.054245	0.001476	0.001591	0.000037	0.282743	0.000027	332	5.94	732.21	961.56
BU-17-08	0.030191	0.000605	0.000982	0.000015	0.282734	0.000027	391	7.01	733.57	938.80
BU-17-09	0.032071	0.001670	0.001012	0.000043	0.282661	0.000026	342	3.38	836.81	1132.60
BU-17-21	0.059194	0.001287	0.001918	0.000030	0.282733	0.000027	348	5.84	753.52	980.25

(*continued on next page*)

Table 4 (*continued*)

Sample	Isotopic ratios						Corrected age			
Akcha biotite gabbro	$^{176}Yb/^{177}Hf$(corr)	2σ	$^{176}Lu/^{177}Hf$(corr)	2σ	$^{176}Hf/^{177}Hf$(corr)	2σ	Age	eHf(t)	TDM1 (Ma)	TDM2(Ma)
BU-17-22	0.063508	0.001180	0.002087	0.000051	0.282695	0.000029	367	4.83	812.99	1059.11
Kalmakyr gabbro										
KLMK-01	0.042706	0.000556	0.001191	0.000025	0.282720	0.000028	333	5.22	757.84	1008.56
KLMK-02	0.039197	0.001552	0.001197	0.000069	0.282689	0.000024	338	4.23	801.89	1075.54
KLMK-05	0.034851	0.001746	0.001040	0.000040	0.282748	0.000026	334	6.28	714.36	941.29
KLMK-07	0.035648	0.000287	0.000982	0.000004	0.282802	0.000026	336	8.25	636.87	817.12
KLMK-09	0.034374	0.000118	0.000943	0.000008	0.282741	0.000027	340	6.17	723.24	953.47
KLMK-10	0.054625	0.000327	0.001652	0.000022	0.282744	0.000028	360	6.52	733.14	945.99
KLMK-11	0.059049	0.000334	0.001814	0.000026	0.282730	0.000027	336	5.49	756.28	993.12
KLMK-13	0.039674	0.000253	0.001120	0.000014	0.282756	0.000027	339	6.64	705.25	922.49
KLMK-16	0.040651	0.000260	0.001125	0.000012	0.282714	0.000025	336	5.09	764.55	1018.67
KLMK-17	0.042378	0.000725	0.001141	0.000015	0.282748	0.000026	352	6.65	716.16	931.85
KLMK-18	0.035563	0.000145	0.000977	0.000005	0.282720	0.000025	343	5.50	752.81	998.41
KLMK-19	0.041111	0.000717	0.001112	0.000012	0.282668	0.000024	359	3.96	829.57	1108.87
KLMK-20	0.044590	0.000548	0.001281	0.000013	0.282683	0.000027	345	4.16	811.59	1085.16

low SiO_2 and relatively high Mg# values (41–61) implying that they dominantly originated from a mantle source, and preclude their derivation from the eclogite-derived and subducted oceanic crust-derived melts (Castillo, 2012; Patiño Douce, 1995, 1997; Richards and Kerrich, 2007; Rudnick and Gao, 2003). This inference is also supported by the relatively depleted Sr-Nd-Hf isotopic compositions of the gabbroic rocks, i.e. $(^{87}Sr/^{86}Sr)_i$ from 0.7044 to 0.7056, $\varepsilon_{Nd(t)}$ values from −1.59 to 1.68, and $\varepsilon_{Hf(t)}$ values from 3.38 to 9.96. Even taking crustal contamination into consideration, the depleted Sr-Nd-Hf isotopes suggest that the gabbroic magmas were derived from a depleted asthenospheric mantle source. In addition, the high LILE/HFSE ratios displayed by the gabbroic rocks are generally ascribed to fluids released from the dehydration of subducted oceanic plate (Bau and Knittel, 1993; Seghedi et al., 2001). This is also reflected by the abundance of biotite and amphibole (Munteanu et al., 2010), and supported by the high water contents in melts, i.e. 4.9–5.3 wt% for Akcha biotite gabbro and 5.6–6.8 wt% for Beleuti gabbro. In summary, the gabbroic rocks are suggested to be derived from a depleted mantle wedge, modified by slab-released fluids with minor crustal contamination during ascent and/or in the crustal magma chamber.

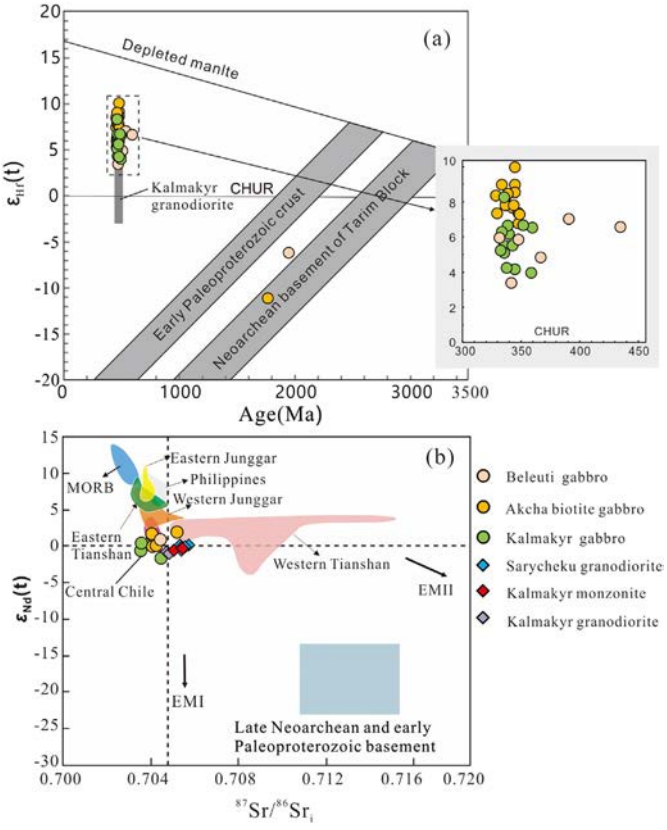

Fig. 9. (a) Age vs. $\varepsilon_{Hf(t)}$ diagram for the analyzed zircons from the gabbroic rocks in the Kurama magmatic arc. Data source: $\varepsilon_{Hf(t)}$ values of the Kalmakyr granodiorite is from Zhao et al. (2017), ore-bearing porphyries from Sarycheku (granodiorite) and Kalmakyr (granodiorite and monzonite) deposits are from Cheng et al. (2018), evolution of the early Paleoproterozoic crust and Neoarchean basement of Tarim Block is from Long et al. (2010, 2011) and Ge et al. (2012), respectively. CHUR = chondritic uniform reservoir. (b) Sr—Nd isotopic compositions of the gabbroic rocks, in combination with the porphyries from the giant porphyry deposits in the Central Asian Orogenic Belt (modified after Cheng et al., 2018).

6.3. Differentiation process in the Kurama arc system

6.3.1. Relationship between gabbroic rocks and ore-bearing porphyries

Previous studies reported a range of ages for the ore-related intrusions from Kalmakyr and Saricheku deposits (Cheng et al., 2018; Dolgopolova et al., 2016; Seltmann et al., 2011; Zhao et al., 2017). For example, Seltmann et al. (2011) reported zircon SHRIMP U—Pb ages of 315 Ma for granodiorite and 308 Ma for monzonite in the Kalmakyr deposit, and 306 Ma for ore-bearing stock in the Saricheku deposit. Dolgopolova et al. (2016) and Konopelko et al. (2017) conducted detailed Sr-Nd-Pb-Hf isotope mapping and U—Pb zircon SHRIMP dating on the Devonian to Permian granitoid intrusions along the Chatkal-Kurama terrane, and reported ages ranging from 289 to 429 Ma, revealing two paleo-subduction zones during the closure of the Turkestan Ocean, i.e. Early Silurian to Middle Devonian and Early Carboniferous, respectively. Cheng et al. (2018) obtained zircon LA-ICP-MS U—Pb ages of 326 Ma for quartz monzonite, 315 Ma for granodiorite in the Kalmakyr deposit, and 337 Ma for granodiorite in the Sarycheku deposit. Zhao et al. (2017) further divided these porphyries into two episodes, i.e. 330–324 Ma and 316–304 Ma. In this study, the emplacement time of gabbroic intrusions is constrained at ca. 340 Ma, which is older than the age of the ore-bearing porphyries in the Almalyk orefield. Hence, the gabbroic rocks might represent the early stage of the Valerianov-Beltau-Kurama arc.

Geochemically, the lack of evolutionary trends between the gabbroic rocks and ore-bearing porphyries in the Harker diagram does not support derivation of the porphyries by fractionation of gabbroic magmas. In the primitive mantle-normalized trace element spidergrams, the gabbroic rocks and porphyries show distinct patterns, e.g. the latter are characterized by negative anomalies of Ba, Ti, and lack positive anomalies of Sr and negative Zr and Hf anomalies compared to gabbroic rocks, which cannot be interpreted by the magma evolution. As shown in the diagram of La/Sm-La and Ce/Yb-Ce, the roughly parallel correlation patterns for gabbroic rocks and porphyries argue against the fractional

Table 5
The Rb—Sr and Sm—Nd isotopic compositions of the gabbroic intrusions in the Valerianov-Beltau-Kurama magmatic arc, Uzbekistan.

Sample	Rb(ppm)	Sr(ppm)	$^{87}Rb/^{86}Sr$	$^{87}Sr/^{86}Sr$	$(^{87}Sr/^{86}Sr)t$	T	Sm(ppm)	Nd(ppm)	$^{147}Sm/^{144}Nd$	$^{143}Nd/^{144}Nd$	$(^{143}Nd/^{144}Nd)t$	εNd(t)
Beleuti gabbro												
Bu-8	38	660	0.166559	0.70636	0.705554	340	1.75	7.79	0.13581245	0.51254881	0.51224648	0.90
Bu-9	43	555	0.224137	0.706552	0.705468	340						
BU-12	11.3	629	0.051968	0.705932	0.705681	340						
BU-14	8.55	660	0.037473	0.705665	0.705484	340						
BU-15	8.91	672	0.038354	0.705599	0.705414	340						
Akcha biotite gabbro												
Ak-5	137	181	2.191938	0.717118	0.70651	340	5.2	26	0.12091248	0.51256971	0.51230055	1.96
Ak-6	34.4	515	0.19323	0.706242	0.705306	340	4.33	20.1	0.13023437	0.51249761	0.5122077	0.14
Ak-7	50.6	518	0.282588	0.706428	0.705061	340	5.01	25.9	0.11694368	0.51254697	0.51228664	1.68
AK-8	50.7	493	0.297507	0.706505	0.705065	340	4.64	23.4	0.1198784	0.51254703	0.51228017	1.56
Ak-10	52.7	657	0.232049	0.706492	0.705369	340						
Kalmakyr gabbro												
Km-9	90.4	703	0.372037	0.707379	0.705605	335	2.88	13.9	0.12525684	0.51240012	0.51212539	−1.59
Km-10	202	437	1.337794	0.710828	0.704449	335	2.17	10.7	0.12260552	0.51250064	0.51223173	0.49
Km-2	127	272	1.351314	0.710876	0.704432	335	5.42	27.5	0.11915009	0.51243907	0.51217773	−0.57

Notes: The $^{87}Sr/^{86}Sr$ and $^{143}Nd/^{144}Nd$ ratios were corrected to $^{86}Sr/^{88}Sr = 0.1194$ and $^{146}Nd/^{144}Nd = 0.7219$, respectively. $\varepsilon_{Nd(t)} = [\{(^{143}Nd/^{144}Nd)s/(^{143}Nd/^{144}Nd)_{CHUR}\} - 1] \times 10^4$, with $(^{143}Nd/^{144}Nd)_{CHUR} = 0.512638$. $T_{2DM} = 1/\lambda_{Sm} \times \ln\{1 + [(^{143}Nd/^{144}Nd)s - (^{143}Nd/^{144}Nd)_{DM} - [(^{147}Sm/^{144}Nd)s - (^{147}Sm/^{144}Nd)c)(e^{\lambda t} - 1)]/[(^{147}Sm/^{144}Nd)c - (^{147}Sm/^{144}Nd)_{DM}]\}$, using $\lambda_{Sm} = 6.54 \times 10^{-12}$, $(^{143}Nd/^{144}Nd)_{DM} = 0.513151$, $(^{147}Sm/^{144}Nd)_{DM} = 0.2137$, $(^{147}Sm/^{144}Nd)c = 0.118$. $(^{147}Sm/^{144}Nd)_m$ and $(^{143}Nd/^{144}Nd)_m$ are the samples of this study. Initial Sr and Nd isotope ratios calculated at 339 Ma, 339 Ma and 335 Ma for the Beleuti gabbro, Akcha biotite gabbro and Kalmakyr gabbro, respectively.

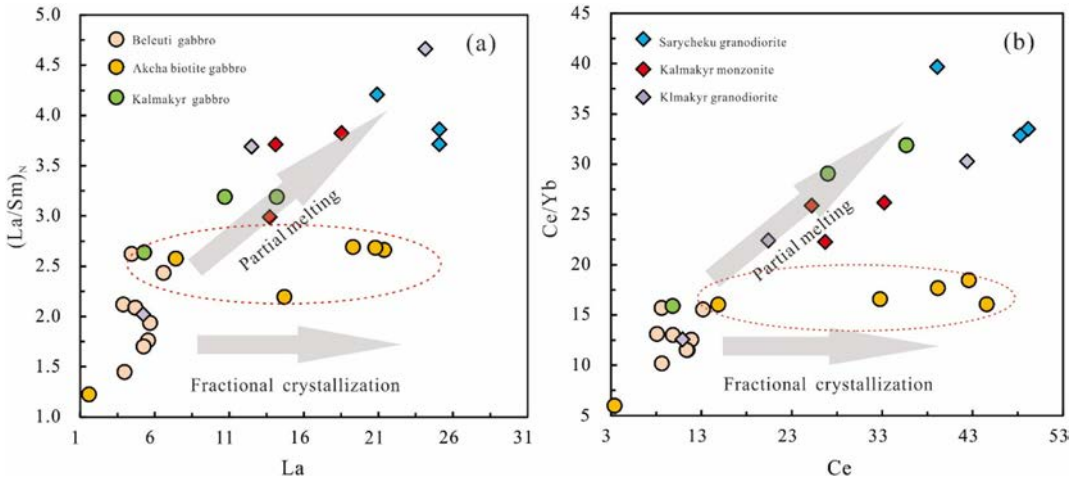

Fig. 10. (a) $(La/Sm)_N$ vs. La, and (b) Ce/Yb vs. Ce diagrams. Data source: ore-bearing porphyries from Sarycheku (granodiorite) and Kalmakyr (granodiorite and monzonite) deposits are from Cheng et al. (2018).

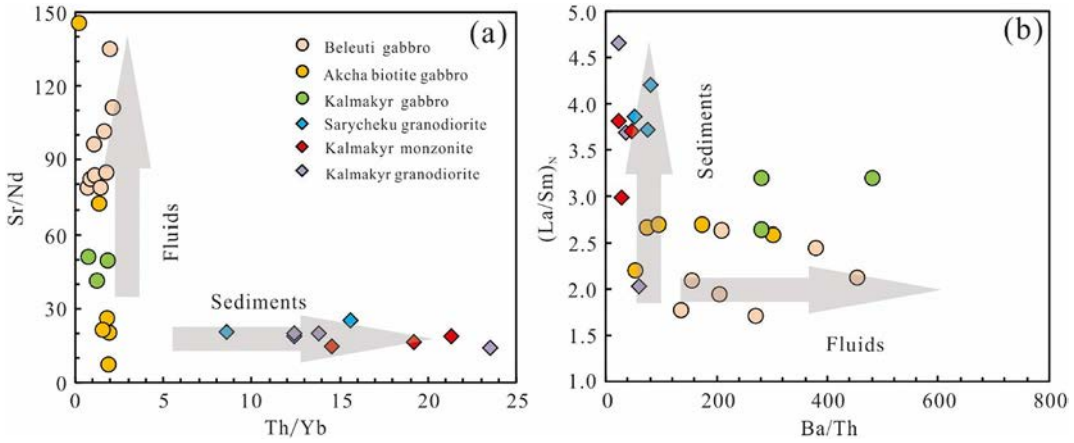

Fig. 11. (a) Diagrams of whole-rock Sr/Nd vs. Th/Yb ratios, and (b) $(La/Sm)_N$ vs. Ba/Th ratios. Data source: ore-bearing porphyries from Sarycheku (granodiorite) and Kalmakyr (granodiorite and monzonite) deposits are from Cheng et al. (2018).

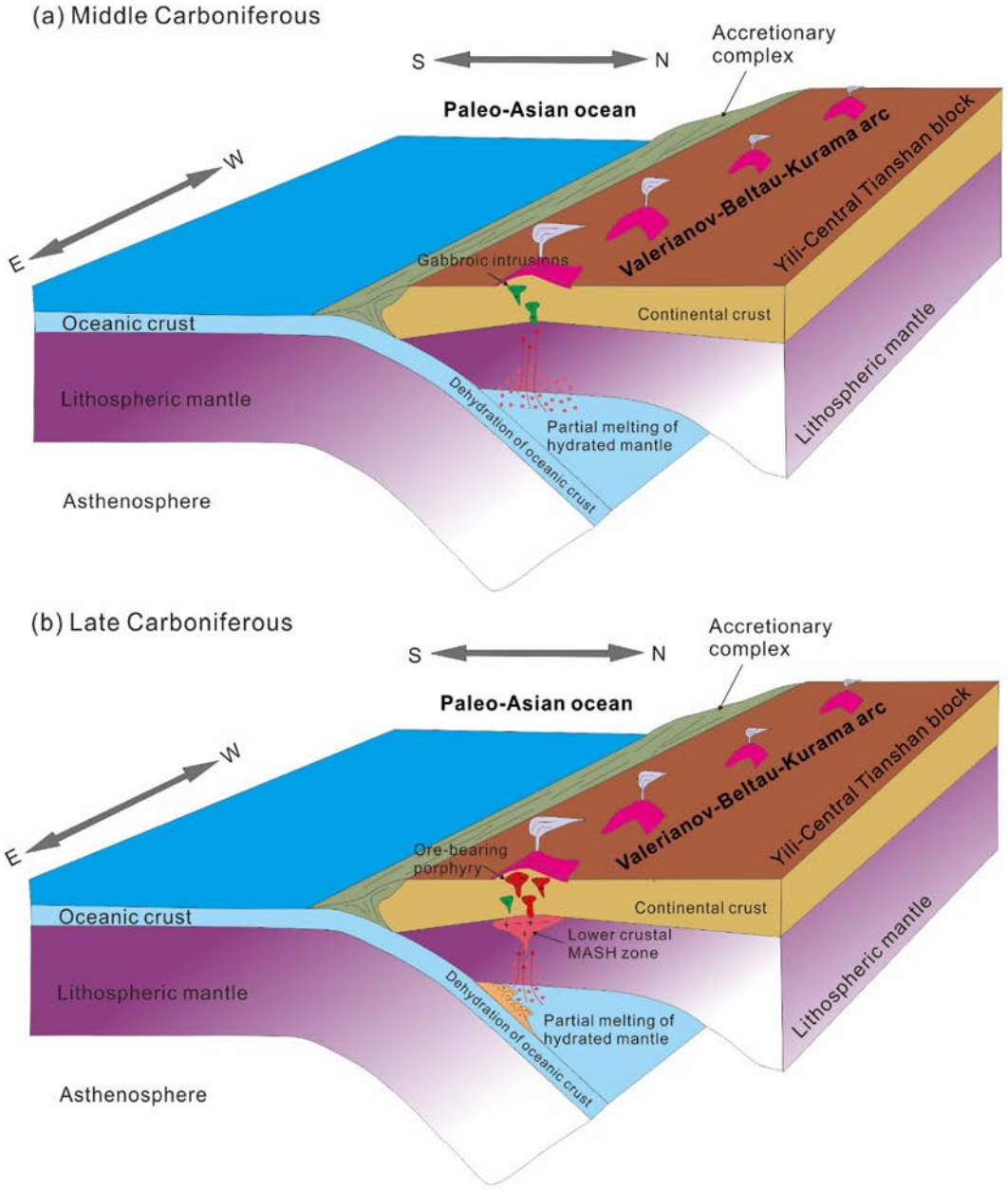

Fig. 12. Genetic model proposed in this study (modified after Cheng et al., 2018). (a) In the Middle Carboniferous, the oceanic plate of Turkestan ocean subducted northward beneath the Middle Tianshan plate. The mantle wedge was modified by fluids from the subducted slab, and the gabbroic rocks were formed from the partial melting of the "wet" mantle wedge with the emplacement age of ca. 340 Ma; (b) In the Late Carboniferous, sediments were involved, and oxygen fugacity was elevated in the mantle wedge. The ore-bearing porphyries (granodiorite and monzonite) were generated through a MASH process in a more mature arc environment.

crystallization of a parental mafic magma in the generation of these porphyries (Fig. 10). These porphyries have higher K_2O contents and show peraluminous features, indicating a higher arc maturity than gabbroic intrusions. In addition, in the AFM diagram, the gabbroic rocks are characterized by tholeiitic evolution trend, whereas the porphyries typically display calc-alkalic trend (Fig. 8b). Furthermore, as shown in Fig. 9, the gabbroic samples are high in Sr/Nd and Ba/Th ratios, but low in Th/Yb and $(La/Sm)_N$ ratios, suggesting the predominant role of fluids in transporting these trace elements (Fig. 11; Elliott, 2003). In comparison, most of the porphyries have contrasting geochemical ratios and are consistent with sediment input in the magma source (Fig. 11). These could either be related to a mantle source modified by subducted sediment-derived melts, or crustal contamination in the MASH zone (Hildreth and Moorbath, 1988; Kemp et al., 2007; Richards, 2011b). Moreover, porphyries have distinct Sr—Nd isotopic composition, in which Sr—Nd isotopes of gabbroic rocks are more depleted than porphyries. On the basis of these data, we suggest that the porphyries were derived from a more evolved continental arc compared to the gabbroic rocks.

6.3.2. Implications for the generation of giant porphyry Cu–Au deposits

Most giant porphyry copper deposits along the Andean Mountain (e.g. Los Pelambres and El Teniente porphyry copper deposits) are suggested to be derived from the slab-melting melts of young oceanic plate, i.e. adakite magmatism (Kay et al., 2005; Reich et al., 2003; Sun et al., 2015). However, this view is debated, because some other mechanisms could also be responsible for the generation of giant porphyry Cu—Au deposits, e.g. MASH process (Richards, 2011a). Our study shows the significance of arc maturity in the formation of giant porphyry deposits,

passing through immature arc to mature arc. Cheng et al. (2018) also proposed that the porphyries in Almalyk orefield are not typical adakite, and therefore, slab melting is not an essential factor.

The subducted slabs transferred the fluids, melts and sediments into mantle wedge, raising the oxidation state to typically 1 or 2 log units above FMQ, enabling more sulfur to be dissolved in the magmas in sulfate form and thus enrich the mineralization (Richards, 2011b, 2015). The empirical formula based on the amphibole yields oxygen fugacity of Log $f O_2 = -13.3$ to -13.8 and water contents of 4.9–5.3 wt% for Akcha biotite gabbro, and oxygen fugacity of Log $f O_2 = -10.1$ to -13.9 and water contents of 5.6–6.8 wt% for Beleuti gabbro (Ridolfi et al., 2010), which are generally consistent with the zircon Ce^{4+}/Ce^{3+} ratios and Ce/Nd values. Notably, Ce/Nd values for Akcha biotite gabbro (avg. 6.7), Beleuti gabbro (avg. 7.2) and Kalmakyr gabbro (avg. 9.0) are lower than those of the porphyries (36.8 for granodiorite) in Kalmakyr deposits (Zhao et al., 2017). Zircon Ce^{4+}/Ce^{3+} ratios of Akcha biotite gabbro (avg. 74), Beleuti gabbro (avg. 71) and Kalmakyr gabbro (avg. 141) are also lower than those of the ore-bearing porphyries (avg. 890) in the Kalmakyr deposits reported by Zhao et al. (2017). Moreover, in the plot of $10^4/T$ vs. Ce^{4+}/Ce^{3+}, most of the gabbroic rocks fall in the field lower range as compared to the porphyries from the giant porphyry deposits in the Central Asian Orogenic Belt (Fig. 8a). Thus, from the gabbroic intrusions to ore-related porphyries, the oxidation state in the subduction regime displays a progressive increase during arc development.

Richards (2003) demonstrated that giant porphyry Cu deposits around the world commonly occur at the culmination of arc tectonomagmatic cycles. Richards et al. (2011) proposed that the key to this process might be the arc maturity, and a long-lived arc magmatism along the subduction zone is necessary to form more geochemically evolved and more hydrous magmas. Hence, a prolonged mature arc is a prerequisite for generating fertile magmatic features, which is also consistent with the porphyry Cu deposits in the Valerianov-Beltau-Kurama magmatic arc. Based on the geological and geochemical observations, we propose a tectonic model for the Valerianov-Beltau-Kurama arc belt, which includes two stages as follows (Fig. 12). (1) In the Middle Carboniferous, during the closure of Turkestan Ocean, the oceanic plate subducted northward beneath the Middle Tianshan plate. The fluids derived from the dehydration of subducted slab modified the mantle wedge and the fluid-rock interaction generated the melts of the gabbroic rocks which were emplaced at ca. 340 Ma. 2) In the Late Carboniferous, the magma derived from mantle wedge experienced the MASH process in the thickened crust. The occurrence of ore-bearing porphyries (granodiorite and monzonite) indicates that they were emplaced in a more mature arc environment, and magma compositions are also chemically evolved.

7. Conclusion

The Akcha biotite gabbro is composed of plagioclase and biotite, whereas the Beleuti and Kalmakyr gabbro are dominated by plagioclase and amphibole. Zircon LA-ICP-MS U—Pb dating reveals that the gabbroic rocks were emplaced at ca. 340 Ma, earlier than the ore-bearing porphyries in the Almalyk orefield. These rocks represent an early stage of the Valerianov-Beltau-Kurama immature arc. High Mg#, low SiO_2 contents and high LILE/HFSE ratios reveal that they are derived from the partial melting of the mantle wedge modified by slab-released fluids. The amphibole chemistry yields high water contents of 4.9–5.3 wt% for Akcha biotite gabbro, and 5.6–6.8 wt% for Beleuti gabbro. However, the oxygen fugacity estimated by zircon Ce/Nd, Ce^{4+}/Ce^{3+} ratios is lower than those of the porphyries from the giant porphyry deposits in Central Asia Orogenic Belt. From the gabbroic rocks to porphyries, the arc maturity plays an important role in controlling the generation of the porphyry Cu deposits in the Valerianov-Beltau-Kurama magmatic arc. The elevated arc maturity, as documented by increasing K_2O contents, A/CNK values and transition from tholeiitic to calc-alkalic magma compositions, were conducive for the formation of ore mineralization.

Acknowledgement

We thank Lithos Editor-in-Chief Prof. Nelson Eby and two anonymous referees for their valuable comments which greatly improved an earlier version of this paper. We thank the Institute of Geology and Geophysics, Academy of Sciences of Uzbekistan for our field work support. Financial support for this work was provided by the National Natural Science Foundation of China (41390442 and 41472060).

Appendix A. Supplementary data

Supplementary data to this article can be found online at https://doi.org/10.1016/j.lithos.2018.08.039.

References

Allen, M.B., Windley, B.F., Zhang, C., 1992. Palaeozoic collisional tectonics and magmatism of the Chinese Tien Shan, Central Asia. Tectonophysics 220, 89–115.
Altherr, R., Topuz, G., Siebel, W., Şen, C., Meyer, H.P., Satir, M., Lahaye, Y., 2008. Geochemical and Sr-Nd-Pb isotopic characteristics of Paleocene plagioleucitites from the eastern Pontides (NE Turkey). Lithos 105, 149–161.
Andersen, T., 2002. Correction of common lead in U-Pb analyses that do not report ^{204}Pb. Chem. Geol. 192, 59–79.
Ballard, J.R., Palin, M.J., Campbell, I.H., 2002. Relative oxidation states of magmas inferred from $Ce^{(IV)}/Ce^{(III)}$ in zircon: application to porphyry copper deposits of northern Chile. Cont. Mineral. Petrol. 144 (3), 347–364.
Bau, M., Knittel, U., 1993. Significance of slab-derived partial melts and aqueous fluids for the genesis of tholeiitic and calc-alkaline island-arc basalts: evidence from Mt. Arayat, Philippines. Chem. Geol. 105, 233–251.
Biske, Y.S., Seltmann, R., 2010. Paleozoic Tian-Shan as a transitional region between the Rheic and Urals-Turkestan oceans. Gondwana Res. 17 (2–3), 602–613.
Boari, E., Avanzinelli, R., Melluso, L., Giordano, G., Mattei, M., De Benedetti, A.A., Morra, V., Conticelli, S., 2009. Isotope geochemistry (Sr–Nd–Pb) and petrogenesis of leucitebearing volcanic rocks from "Colli Albani" volcano, Roman Magmatic Province, Central Italy: inferences on volcano evolution and magma genesis. Bull. Volcanol. 71, 977–1005.
Briqueu, L., Bougault, H., Joron, J.L., 1984. Quantification of Nb, Ta, Ti and V anomalies in magmas associated with subduction zones: petrogenetic implications. Earth Planet. Sci. Lett. 68, 297–308.
Castillo, P.R., 2012. Adakite petrogenesis. Lithos 134-135, 304–316.
Cheng, Z.G., Zhang, Z.C., Chai, F.M., Hou, T., Santosh, M., Turesebekov, A., Nurtaev, B.S., 2018. Carboniferous porphyry Cu-au deposits in the Almalyk orefield, Uzbekistan: the Sarycheku and Kalmakyr examples. Int. Geol. Rev. 60 (1), 1–20.
Chiaradia, M., 2013. Copper enrichment in arc magmas controlled by overriding plate thickness. Nat. Geosci. https://doi.org/10.1038/NGEO2028.
Chu, N.C., Taylor, R.N., Chavagnac, V., Nesbitt, R.W., Boella, R.M., Milton, J.A., German, C.R., Bayon, G., Burton, K., 2002. Hf isotope ratio analysis using multi-collector inductively coupled plasma mass spectrometry: an evaluation of isobaric interference corrections. J. Anal. Atomic Spectr. 17, 1567–1574.
Cooke, D.R., Hollings, P., Walshe, J.L., 2005. Giant porphyry deposits: characteristics, distribution, and tectonic controls. Econ. Geol. 100 (5), 801–818.
Corfu, F., Hanchar, J.M., Hoskin, P.W.O., Kinny, P., 2003. Atlas of zircon textures. Rev. Mineral. Geochem. 53 (1), 469–500.
Dolgopolova, A., Seltmann, R., Konopelko, D., Biske, Y.S., Shatov, V., Armstrong, R., Belousova, E., Pankhurst, R., Koneev, R., Divaev, F., 2016. Geodynamic evolution of the western Tien Shan, Uzbekistan: Insight from U-Pb SHRIMP geochronology and Sr-Nd-Pb-Hf isotope mapping of granitoids. Gondwana Res. https://doi.org/10.1016/h.gr.2016.10.022.
Ducea, M.N., Saleeby, J.B., Bergantz, G., 2015. The architecture, chemistry, and evolution of continental magmatic Arcs. Ann. Rev. Earth Planet. 43, 299–331.
Elburg, M.A., van Bergen, M., Hoogewerff, J., Foden, J., Vroon, P., Zulkarnain, I., Nasution, A., 2002. Geochemical trends across an arc–continent collision zone: magma sources and slab-wedge transfer processes below the Pantar Strait volcanoes, Indonesia. Geochimica et Cosmochimica Acta 66, 2771–2789.
Elhlou, S., Belousova, E., Griffin, W.L., Pearson, N.J., O'Reilly, S.Y., 2006. Trace element and isotopic composition of GJ-red zircon standard by laser ablation. Geochimica et Cosmochimica Acta 70, A158.
Elliott, T., 2003. Tracers of the slab. In: Eiler, J. (Ed.), Inside the Subduction Factory American Geophysical Union Geophysical Monograph 138, pp. 23–45.
Foster, M.D., 1960. Interpretation of the composition of trioctahedral micas. U S Geological Survey Professional Paper 354 (B), 11–49.
Gao, J., Long, L.L., Klemd, R., Qian, Q., Liu, D.Y., Xiong, X.M., Su, W., Liu, W., Wang, Y.T., Yang, F.Q., 2009. Tectonic evolution of the south Tianshan orogeny and adjacent regions, NW China: Geochemical and age constraints of granitoid rocks. J. Earth Sci. 98 (6), 1221–1238.
Ge, R.F., Zhu, W.B., Wu, H.L., Zheng, B.H., Zhu, X.Q., He, J.W., 2012. The Paleozoic northern margin of the Tarim Craton: passive or active? Lithos 142-43, 1–15.

Golovanov, I.M., Seltmann, R., Kremenetsky, A.A., 2005. The Porphyry Cu–Au/Mo Deposits of Central Euroasia: 2. The Almalyk (Kalmakyr–Dalnee) and Saukbulak Cu–Au Porphyra Systems, Uzbekistan. In: Porter, T.M. (Ed.), Super Porphyry Copper and Gold Deposits: A Global Perspective. Vol. 2. PGC Publishing, Adelaide, pp. 513–523.
Hildreth, W., Moorbath, S., 1988. Crustal contributions to arc magmatism in the Andes of Central Chile. Cont. Mineral. Petrol. 98, 455–489.
Hoskin, P.W.O., Schaltegger, U., 2003. The composition of zircon and igneous and metamorphic petrogenesis. Rev. Mineral. Geochem. 53 (1), 27–62.
Hou, K.J., Li, Y.H., Zou, T.R., Qu, X.M., Shi, Y.R., Xie, G.Q., 2007. Laser ablation-MC-ICP-MS technique for Hf isotope microanalysis of zircon and its geological applications. Acta Petrologica Sinica 23, 2595–2604 (in Chinese with English abstract).
Kay, S.M., Godoy, E., Kurz, A., 2005. Episodic arc migration, crustal thickening, subduction erosion, and magmatism in the south-Central Andes. Geol. Soc. Am. Bull. 117, 67–88.
Kelemen, P.B., Hanghoj, K., Greene, A.R., 2014. One view of the geochemistry of subduction-resecondd magmatic arcs, with an emphasis on primitive andesite and lower crust. Treatise Geochem. 3, 593–659.
Kemp, A.I.S., Hawkesworth, C.J., Foster, G.L., Paterson, B.A., Woodhead, J.D., Hergt, J.M., Gray, C.M., Whitehouse, M.J., 2007. Magmatic and crustal differentiation history of granitic rocks from Hf-O isotopes in zircon. Science 315, 980–983.
Konopelko, D., Seltmann, R., Mamadjanov, Y., Romer, R.L., Rojas-Agramonte, Y., Jeffries, T., Fidaev, D., Niyozov, A., 2017. A geotraverse across two paleo-subduction zones in Tien Shan, Tajikistan. Gondwana Res. 47, 110–130.
Koschek, G., 1993. Origin and significance of the SEM cathodoluminescence from zircon. J. Micros. 171, 223–232.
Leake, B.E., Woolley, A.R., Arps, C.E.S., 1997. Nomenclature of amphiboles: Report of the Subcommittee on Amphiboles of the International Miner-alogical Association, Commission on New Mineral and Mineral Names. Am. Mineral. 82, 1019–1037.
Li, C.F., Li, X.H., Li, Q.L., Guo, J.H., Li, J.H., Li, X.H., Yang, Y.H., 2012. Rapid and precise determination of Sr and Nd isotopic ratios in geological samples from the same filament loading by thermal ionization mass spectrometry employing a single-step separation scheme. Anal. Chim. Acta 727, 54–60.
Liu, Y.S., Hu, Z.C., Gao, S., Gunther, D., Xu, J., Gao, C.G., Chen, H.H., 2008. In situ analysis of major and trace elements of anhydrous minerals by LA-ICP-MS without applying an internal standard. Chem. Geol. 257 (1–2), 34–43.
Liu, Y.S., Gao, S., Hu, Z.C., Gao, C.G., Zong, K.Q., Wang, D.B., 2010. Continental and oceanic crust recycling-induced melt-peridotite interactions in the Trans-North China Orogen: U-Pb dating, Hf isotopes and trace elements in zircons from mantle xenoliths. J. Petrol. 51 (1–2), 537–571.
Long, X.P., Yuan, C., Sun, M., Zhao, G.C., Xiao, W.J., Wang, Y.J., Yang, Y.H., Hu, A.Q., 2010. Archean crustal evolution of the northern Tarim Craton, NW China: zircon U-Pb and Hf isotopic constraints. Precambrian Res. 180, 272–284.
Long, X.P., Yuan, C., Sun, M., Kröner, A., Zhao, G.C., Wilde, S., Hu, A.Q., 2011. Reworking of the Tarim Craton by underplating of mantle plume-derived magmas: evidence from Neoproterozoic granitoids in the Kuluketage area, NW China. Precambrian Res. 187, 1–14.
Ludwig, K.R., 2003. User's manual for Isoplot/Ex. Version 3.00: A Geochronological Toolkit for Microsoft Excel. Berkeley Geochronology Center Special Publication 4, 1–70.
MacDonald, R., Hawkesworth, C.J., Heath, E., 2000. The Lesser Antilles volcanic chain: a study in arc magmatism. Earth Sci. Rev. 49, 1–76.
Mao, J.W., Pirajno, F., Lehmann, B., Luo, M.C., Berzina, A., 2014. Distribution of porphyry deposits in the Eurasian continent and their corresponding tectonic settings. J. Asian Earth Sci. 79, 576–584.
McBirney, A.R., Creaser, R.A., 2003. The Skaergaard layered series, part VII: Sr and Nd isotopes. J. Petrol. 44, 757–771.
McDonough, W.F., Sun, S.S., 1995. The composition of the Earth. Chem. Geol. 120, 2523–2553.
Muir, R.J., Weaver, S.D., Bradshaw, J.D., Eby, G.N., Evans, J.A., 1995. The cretaceous Separation Point batholith, New Zealand: granitoid magmas formed by melting of mafic lithosphere. Geol. Soc. London 152, 689–701.
Munteanu, M., Wilson, A., Yao, Y., Harris, C., Chunnett, G., Luo, Y.N., 2010. The Tongde dioritic pluton (Sichuan, SW China) and its geotectonic setting: regional implications of a local-scale study. Gondwana Res. 18, 455–465.
Namur, O., Charlier, B., Toplis, M.J., Higgins, M.D., Liégeois, J.P., Vander Auwera, J., 2010. Crystallization sequence and magma chamber processes in the ferrobasaltic Septlles layered intrusion, Canada. J. Petrol. 51, 1203–1236.
Norrish, K., Chappell, B.W., 1997. X-ray fluorescence spectrometry. In: Zussman, J. (Ed.), Physical Methods in Determinative Mineralogy, 2nd edition Academic Press, New York, pp. 201–272.
Ouyang, H., Mao, J., Zhou, Z., Su, H., 2015. Late Mesozoic metallogeny and intracontinental magmatism, southern Great Xing'an Range, northeastern China. Gondwana Res. 27, 1153–1172.
Patiño Douce, A.E., 1995. Dehydration-melting of biotite gneiss and quartz amphibolite from 3 to 15 kbar. J. Petrol. 36, 707–738.
Patiño Douce, A.E., 1997. Generation of metaluminous A-type granites by low-pressure melting of calc-alkaline granitoids. Geology 25, 743–746.
Peccerillo, A., Taylor, S.R., 1976. Geochemistry of Eocene calc-alkaline volcanic rocks from the Kastamonu area, northern Turkey. Contrib. Mineral. Petrol. 58, 63–81.
Qi, L., Hu, J., Gregoire, D.C., 2000. Determination of trace elements in granites by inductively coupled plasma mass spectrometry. Talanta 51, 507–513.
Reich, Martin, Parada, M.A., Palacios, C., Dietrich, A., Schultz, F., Lehman, B., 2003. Adakite-like signature of late Miocene intrusions at the Los Pelambres giant porphyry copper deposit in the Andes of Central Chile-Metallogenic implications. Mineralium Deposita 38, 876–885.
Richards, J.P., 2003. Tectono-magmatic precursors for porphyry Cu-(Mo-au) deposit formation. Econ. Geol. 98, 1515–1533.
Richards, J.P., 2011a. High Sr/Y arc magmas and porphyry Cu±Mo±au deposits: just add water. Econ. Geol. 106 (7), 1075–1081.
Richards, J.P., 2011b. Magmatic to hydrothermal metal fluxes in convergent and collided margins. Ore Geol. Rev. 40, 1–26.
Richards, J.P., 2015. The oxidation state, and sulfur and Cu contents of arc magmas: implications for metallogeny. Lithos 233, 27–45.
Richards, J.P., Kerrich, R., 2007. Adakite-like rocks: their diverse origins and questionable role in metallogenesis. Econ. Geol. 102, 537–576.
Richards, J.P., Spell, T., Rameh, E., Razique, A., Fletcher, T., 2011. High Sr/Y magmas reflect arc maturity, high magmatic water content, and porphyry Cu±Mo±au potential: examples from the Tethyan arcs of central and eastern Iran and western Pakistan. Econ. Geol. 107, 295–332.
Ridolfi, F., Renzulli, A., Puerini, M., 2010. Stability and chemical equilibrium of amphibole in calc-alkaline magmas: an overview, new thermobarometric formulations and application to subduction-related volcanoes. Contr. Mineral. Petrol. 160 (1), 45–66.
Rudnick, R.L., 1995. Making continental crust. Nature 378, 571–578.
Rudnick, R.L., Gao, S., 2003. The composition of the continental crust. In: Rudnick, R.L. (Ed.), The Crust. Elsevier-Pergamon, Oxford, pp. 1–64.
Salters, V.J.M., Stracke, A., 2004. Composition of the depleted mantle. Geochem. Geophys. Geosyst. https://doi.org/10.1029/2003GC000597.
Seghedi, I., Downes, H., Pécskay, Z., Thirlwall, M.F., Szakács, A., Prychodko, M., Mattey, D., 2001. Magmagenesis in a subduction-related post-collisional volcanic arc segment: the Ukrainian Carpathians. Lithos 57 (4), 237–262.
Seltmann, R., Konopelko, D., Biske, G., Divaev, F., Sergeev, S., 2011. Hercynian post-collisional magmatism in the context of Paleozoic magmatic evolution of the Tien Shan orogenic belt. J. Asian Earth Sci. 42 (5), 821–838.
Seltmann, R., Porter, T.M., Pirajno, F., 2014. Geodynamics and metallogeny of the central Eurasian Porphyry and related epithermal mineral systems: a Review. J. Asian Earth Sci. 79, 810–841.
Shen, P., Hattori, K., Pan, H.d., Jackson, S., Seitmuratova, E., 2015. Oxidation condition and metal fertility of granitic magmas: Zircon trace-element data from porphyry Cu deposits in the Central Asian orogenic belt. Econ. Geol. 110 (7), 1861–1878.
Sillitoe, R.H., 2010. Porphyry copper systems. Econ. Geol. 105, 3–41.
Sun, S.S., McDonough, W.F., 1989. Chemical and isotopic systematic of oceanic basalts: implications for mantle composition and process. In: Saunders, A.D., Norry, M.J. (Eds.), Magmatism in Ocean Basins. Vol. 42. Geological Society London Special Publications, pp. 313–345.
Sun, W.D., Zhang, H., Ling, M.X., Ding, X., Chung, S.L., Zhou, J.B., Yang, X.Y., Fan, W.M., 2011. The genetic association of adakites and Cu–au ore deposits. Int. Geol. Rev. 53 (5–6), 691–703.
Sun, W.D., Huang, R.F., Li, H., Hu, Y.B., Zhang, C.C., Sun, S.J., Zhang, L.P., Ding, X., Li, C.Y., Zartman, R.E., Ling, M.X., 2015. Porphyry deposits and oxidized magmas. Ore Geol. Rev. 65, 97–131.
Windley, B.F., Alexeiev, D., Xiao, W., Kröner, A., Badarch, G., 2007. Tectonic models for accretion of the Central Asian Orogenic Belt. J. Geol. Soc. London 164, 31–47.
Wu, C., Chen, H.Y., Hollings, P., Xu, D., Liang, P., Han, J.S., Xiao, B., Cai, K.D., Liu, Z.J., Qi, Y.K., 2015. Magmatic sequences in the Halasu Cu Belt, NW China: Trigger for he Paleozoic porphyry Cu mineralization in the Chinese Altay-East Junggar. Ore Geol. Rev. 71, 373–404.
Xiao, W.J., Santosh, M., 2014. The western Central Asian Orogenic Belt: a window to accretionary orogenesis and continental growth. Gondwana Res. 25, 1429–1444.
Xiao, W.J., Huang, B.C., Han, C.M., Sun, S., Li, J.L., 2010. A review of the western part of the Altaids: a key to understanding the architecture of accretionary orogens. Gondwana Res. 18, 253–273.
Xiao, W.J., Windley, B.F., Allen, M., Han, C.M., 2013. Paleozoic multiple accretionary and collisional tectonics of the Chinese Tianshan orogenic collage. Gondwana Res. 23, 1316–1341.
Xue, C.J., Zhao, X.B., Mo, X.X., Chen, Y.C., Dong, L.H., Gu, X.X., Zhang, Z.C., Nurtaev, B., Pak, N., Li, Z.D., Wang, X.L., Zhang, G.Z., Yaxiaer, Y., Feng, B., Zu, B., Liu, J.Y., 2014a. Tectonic-Metallogenic Evolution of Western Tianshan Giant Au-Cu-Zn-Pb Metallogenic Belt and Prospecting Orietation. Acta Geosci. Sinica 88 (12), 2490–2531 (in Chinese with Englisj abstract).
Xue, C.J., Zhao, X.B., Mo, X.X., Dong, L.H., Gu, X.X., Nurtaev, B., Pak, N., Zhang, Z.C., Wang, X. L., Zu, B., Zhang, G.Z., Feng, B., Liu, J.Y., 2014b. Asian Gold Belt in western Tianshan and its dynamic setting, metallogenic control and exploration. Front. Earth Sci. 21 (5), 128–155.
Yang, F.Q., Mao, J.W., Pirajno, F., Yan, S.H., Liu, G.R., Zhou, G., Zhang, Z.X., Liu, F., Geng, X.X., Guo, C.L., 2012. A review of the geological characteristics and geodynamic setting of late Paleozoic porphyry copper deposits in the Junggar region, Xinjiang Uygur Autonomous Region, Northwest China. J. Asian Earth Sci. 49, 80–98.
Yang, F.Q., Chai, F.M., Zhang, Z.X., Geng, X.X., Li, Q., 2014. Zircon U-Pb geochronology, geochemistry, and Sr-Nd-Hf isotopes of granitoids in the Yulekenhalasu copper ore district, northern Junggar, China: Petrogenesis and tectonic implications. Lithos 190-191, 85–103.
Zhao, Z.Y., Zhang, Z.C., Santosh, M., Huang, H., Cheng, Z.G., Ye, J.C., 2015. Early Paleozoic magmatic record from the northern margin of the Tarim Craton: further insights on the evolution of the Central Asian Orogenic Belt. Gondwana Res. https://doi.org/10.1016/j.gr.2014.04. 007.
Zhao, X.B., Xue, C.J., Chi, G.X., Mo, X.X., Nurtaev, B., Zhang, G.Z., 2017. Zircon and molybdenite geochronology and geochemistry of the Kalmakyr porphyry Cu-au deposit, Almalyk district, Uzbekistan: Implications for mineralization processes. Ore Geol. Rev. 86, 807–824.